

DESIGN OF A SPLIT HOPKINSON PRESSURE BAR FACILITY FOR DYNAMIC
MATERIAL CHARACTERIZATION

By JOSEPH R. SPANIOL

A thesis submitted to the

School of Graduate Studies

Rutgers, The State University of New Jersey

In partial fulfillment of the requirements

For the degree of

Master of Science

Graduate Program in Mechanical and Aerospace Engineering

Written under the direction of

Assimina A. Pelegri

And approved by

New Brunswick, New Jersey

October 2019

ABSTRACT OF THE THESIS

DESIGN OF A SPLIT HOPKINSON PRESSURE BAR FACILITY FOR DYNAMIC
MATERIAL CHARACTERIZATION

By JOSEPH R. SPANIOL

Thesis Director:

Dr. Assimina A. Pelegri

It is important to know the mechanical response of materials over a full range of strain rates. In machining and stamping, or in ballistic type events such as bullet penetration, shell impacts, and explosive blasts, strain rates of 100 s^{-1} to $10,000 \text{ s}^{-1}$ or even higher for hyper-velocity impacts, are achieved. A Split Hopkinson Pressure Bar facility is generally used to study the mechanical response of materials at these strain rates. The Split Hopkinson Pressure Bar produces precise data which can be used to study the dynamic response of materials. Over the last 70 years the Split Hopkinson Pressure Bar has been subject to many scrupulous studies which push the boundaries of materials it can test. In this thesis, the design of a compressive Split Hopkinson Pressure Bar facility is presented. The Split Hopkinson Pressure Bar is designed to obey the fundamental assumptions: one-dimensional and undispersed wave propagation as well as uniaxial loading of the specimen. Each subsystem of the compressive Split Hopkinson Pressure Bar is closely examined to outline its role in obeying these assumptions as well as its role in obtaining accurate data acquisition, then a design of each subsystem is presented. The presented facility improves accuracy, functionality, and ease of operation compared to previous work. Improvements

in strain gage design increased the maximum attainable impact velocity from 40 m/s to at least 50 m/s. The Split Hopkinson Pressure Bar facility is thoroughly tested to verify the design. The dynamic response of aluminum 6061-T6511 is tested between strain rates of $1,000 \text{ s}^{-1}$ and $6,300 \text{ s}^{-1}$ to verify the accuracy of the facility. Testing showed that the response of 6061-T6511 is strain rate dependent which is consistent with literature. The flow stress of 6061-T6511 increases as strain rate increases from 350 MPa to 400 MPa at a rate of about 0.009 MPa-s. The dynamic response of polycarbonate is reported at strain rates between $1,000 \text{ s}^{-1}$ and $7,000 \text{ s}^{-1}$. The flow stress increases by about 8.2% over the range of strain rates. Super activated carbon and a super activated carbon composite is also studied using aluminum pressure bars, specifically designed for soft materials.

ACKNOWLEDEMENTS

First and foremost, I would like to express my sincerest gratitude to my advisor and mentor Professor Assimina Pelegri for her overwhelming support throughout my education at Rutgers University. Her advice inspired me to take on many leadership roles during my time at Rutgers which has been instrumental in deciding my future career aspirations. I could not have been more fortunate to have her as my advisor.

I would like to thank everyone that has helped with the project: Professor Edward DeMauro for his relentless engagement in the design of data acquisition system and willingness to support my project, and Max Tenorio, Andrea Olarte, and Asaad Shaikh for their respective contributions and for taking on the responsibilities of operating the facility after my departure.

I would like to thank my mentor Mr. Paul Pickard for his advice in designing and manufacturing the Split Hopkinson Pressure Bar and for nurturing my development and success over the last few years.

I would also like to acknowledge my thesis committee: Dr. Assimina Pelegri, Dr. Edward DeMauro, and Dr. Rajiv Malhotra for their time in my defense.

Lastly, I would like to thank my friends and family who have supported me throughout my higher education, especially my parents, David and Delan, and my brother and sister, Mike and Anna.

TABLE OF CONTENTS

ABSTRACT OF THE THESIS.....	ii
ACKNOWLEDEMENTS.....	iv
TABLE OF CONTENTS.....	v
LIST OF TABLES	vii
LIST OF FIGURES	viii
LIST OF ACRONYMS AND SYMBOLS	xi
Chapter 1 – INTRODUCTION.....	1
1.1 – General Description of the Split Hopkinson Pressure Bar	3
1.2 – Historical Aspect.....	6
1.3 – Current Research.....	7
Chapter 2 – THEORY	9
2.1 – Theory of the Split-Hopkinson Pressure Bar.....	9
Chapter 3 – EXPERIMENTAL DESIGN AND SETUP.....	17
3.1 – Design of Split Hopkinson Pressure Bar.....	17
3.1.1 - Striker Launching System	17
3.1.2 - Pressure Bars	26
3.1.3 - Strain Gages and Signal Conditioning.....	29
3.1.4 - Bar Alignment	37
3.1.5 - Momentum Trap.....	40
3.1.6 – Structure	41
3.2 – Specimen Design	42
3.3 – Data Processing.....	43
Chapter 4 – RESULTS AND DISCUSSION	47
4.1 – System Calibration.....	47
4.2 – Pulse Shaping Effects on Incident Pulse and Dispersion	52
4.3 – Dynamic Response of Al 6061-T6511.....	56
4.4 – Dynamic Response of Polycarbonate.....	62
4.5 – Dynamic Response of SAC and SAC + CNT	66
Chapter 5 – CONCLUSIONS	71
Chapter 6 – FUTURE WORK	73
APPENDICES	74

REFERENCES.....	77
-----------------	----

LIST OF TABLES

Table 1: Table of pressure bar sets	29
Table 2: Experimentally determined wave speed of C350 pressure bars. The uncertainties represent the inaccuracy in the data acquisition equipment.....	48
Table 3: Table of 6061-T6511 test specimens.	56
Table 4: Table of Polycarbonate specimens.....	62
Table 5: Table of Super Activated Carbon (SAC) specimens.....	67
Table 6: Table of Super Activated Carbon + CNT (SAC + CNT) specimens.	67

LIST OF FIGURES

Figure 1.1: Controlled experimental techniques used to study materials at various strain rate regions. Kolsky bars are the general name for a Split Hopkinson Pressure Bar. Reproduced from Ramesh, K.T [1].	2
Figure 1.2: General design schematic of a compressive Split Hopkinson Pressure Bar.	4
Figure 1.3: B. Hopkinson's original pressure bar experiment. Reproduced from Hopkinson [3].	6
Figure 2.1: Wave propagation of an elastic rod impacting a rigid wall.	9
Figure 2.2: Lagrangian diagram for a Split Hopkinson Pressure Bar shows the propagation of the stress wave through time. The x-axis represents position along the SHPB and y-axis represents time.	11
Figure 2.3: Schematic of specimen and strain pulses. 1 indicates incident bar-specimen interface. 2 indicated transmission bar-specimen interface.	12
Figure 2.4: Example of a Wheatstone bridge circuit in a quarter bridge configuration.	15
Figure 3.1: Time step convergence of the gas gun numerical model. The time step is chosen such that, $v_{i+1} - v_i < 0.01 \text{ m/s}$. Convergence study shows that a maximum time step of $7.5 \mu\text{s}$ should be used.	19
Figure 3.2: Convergence of analytical solution to numerical solution with varying reservoir volume at initial pressure of 136 atm. The red circle indicates the reservoir volume that is used in the design, 0.0035 m^3 . The analytical solution overestimates the velocity by 1.25%.	20
Figure 3.3: Reservoir tank of the striker propelling system. Control volume is 0.0035 m^3 .	21
Figure 3.4: Barrel of the SHPB launching system. Two 76 mm slits are machined towards the exhaust end of the barrel. The barrel is held down by three adjustable stage clamps.	22
Figure 3.5: Striker velocity as a function of initial reservoir pressure with numerical and analytical solutions. For lower pressures, the analytical solution may be used to accurately predict velocity.	23
Figure 3.6: Pneumatic control panel to control the initial reservoir pressure.	24
Figure 3.7: Release valve and manual safety shut-off valve.	25
Figure 3.8: The strain gage measures the average strain over its gage length.	30
Figure 3.9: Examples of broken connecting wires on incident bar terminal pad. A. Broken connecting wire for axial gage. B. Broken connecting wire for transverse gage V+ excitation wire.	31
Figure 3.10: Schematic of a 3-wire quarter Wheatstone bridge. Reproduced from Micro-Measurements Application Note VMM-5.	32
Figure 3.11: Installed strain gage on incident pressure bar.	33
Figure 3.12: Kulite KSC-2 signal conditioners.	34
Figure 3.13: Wheatstone bridge completion circuits for axial and transverse measurements.	34
Figure 3.14: 1. National Instruments cDAQ 9185 chassis with 2. NI 9775 digitizer, 3. NI 9402 DIO, and 4. NI 9205 AIO modules.	35
Figure 3.15: Good axial alignment of pressure bars. Incident and transmitted pulses match and the reflected pulse is close to zero.	38

Figure 3.16: Ceramic lined linear bearing mounted in split pillow block bearing housing. The pillow block housing uses four set screws to adjust the alignment of the bearing. A. Oil port. B. Mounting screws. C. Adjustment set screws.....	39
Figure 3.17: Laser alignment of bearings.	40
Figure 3.18: The momentum trap consists of a bar and shock absorber.	41
Figure 3.19: Comparison of calculated response curves of bonded, dry, and lubricated specimens. Increasing the coefficient of friction significantly increases the stress in the specimen. Reproduced from Bertholf and Karnes [4].	43
Figure 3.20: Translated incident, reflected, and transmitted waves for a polycarbonate specimen.	44
Figure 3.21: Striker velocity determination. Striker crosses laser curtain in 2.141 ± 0.02 ms, resulting in a velocity of 35.6 m/s for a 3” striker bar.	45
Figure 4.1: Bar wave speed calibration for C350 pressure bars. Time between the start of the incident pulse and start of the reflected pulse is used to calculate wave speed.....	47
Figure 4.2: Measured and predicted striker velocities vs. initial pressure. The analytical solution and numerical model are shown. Results for two striker lengths are shown.....	49
Figure 4.3: Example of calibration test with no specimen. Velocity of striker is 22.6 m/s. The amplitude of the incident and transmitted pulses match the amplitude of the theoretical input strain indicating system is in good calibration.	50
Figure 4.4: Example of bad system calibration. The incident and transmitted pulses fall short of the predicted strain value.	50
Figure 4.5: Translated incident, reflected, and transmitted waves during a calibration test. The transmitted and incident waves match in amplitude indicating good calibration. The reflected pulse is very close to zero which indicates the pressure bars are in good alignment.....	51
Figure 4.6: Pulse shaper effect on incident pulse. The strain is normalized by the striker velocity.....	53
Figure 4.7: Pulse shapers reducing the variance between the incident and transmitted pulses.	54
Figure 4.8: Frequency spectrum of a non-pulsed shaped incident pulse and a pulse shaped incident pulse. The pulse shaper acts as a low pass filter.	55
Figure 4.9: A. Pulse shaper loaded on the incident bar. B. Pulse shapers before and after use.....	55
Figure 4.10: Incident and transmitted bar strains from test sample SN 7.....	57
Figure 4.11: Aluminum specimens before and after dynamic compression.....	57
Figure 4.12: Strain in specimen SN 7 over time. Both three and one wave methods are shown. The true strain corrects for the Poisson’s effect.	58
Figure 4.13: Strain rate of test specimen 6061-T6511 SN 7. Constant strain rate is achieved after 40 μ s.	59
Figure 4.14: Dynamic response of 6061-T6511 Aluminum Alloy over a range of strain rates.....	60
Figure 4.15: Flow stress strain rate dependency of 6061-T6511 at 25% strain.	61
Figure 4.16: Peak stress strain rate dependency for 6061-T6511 between 1000 s^{-1} and 3000 s^{-1}	61
Figure 4.17: Polycarbonate specimen before and after SHPB experiment.....	63
Figure 4.18: Dynamic stress-strain curves of Polycarbonate.....	63

Figure 4.19: Stress-strain curves of polycarbonate. Reproduced from Siviour, C. R. et al. [2].	64
Figure 4.20: Flow stress of PC specimens at 12.5% strain at various strain rates.	64
Figure 4.21: Peak stress of PC specimens at various strain rates.....	65
Figure 4.22: Translated strain waves of SAC specimen SN 5. The transmitted signal is very weak compared to the incident and reflected signals, which closely match.....	66
Figure 4.23: Dynamic response of SAC at various strain rates.....	68
Figure 4.24: Dynamic response of SAC + CNT composite.....	69
Figure 4.25: Peak stress versus strain rate for SAC and SAC + CNT.....	70

LIST OF ACRONYMS AND SYMBOLS

SHPB	Split Hopkinson Pressure Bar
c	Wave speed of pressure bar material
c_s	Wave speed of specimen material
E	Elastic modulus of pressure bar material
E_s	Elastic Modulus of specimen material
v_{st}	Velocity of striker bar
m_{st}	Mass of striker bar
A_{st}	Cross-sectional area of striker bar
l	Length of gas gun barrel
ρ	Density of pressure bar material
ϵ_I	Incident strain history
ϵ_R	Reflected strain history
ϵ_T	Transmitted strain history
ϵ_s	Specimen strain history
ϵ	True specimen strain
σ_s	Specimen stress
σ	True specimen stress
$\dot{\epsilon}_s$	Specimen strain rate history
A	Cross-sectional area of pressure bars
A_s	Cross-sectional area of specimen
L_s	Initial length of specimen
d	Diameter of pressure bars
d_s	Diameter of specimen
R_g	Resistance of strain gage
R_l	Resistance of strain gage lead wires
L_g	Gage length of strain gage
L_{II}	Length from incident strain gage to specimen interface
L_{TI}	Length from transmission strain gage to specimen interface
E_i	Excitation voltage
E_0	Sense voltage
f_c	Frequency cutoff

Chapter 1 – INTRODUCTION

The dynamic behavior of a material and its mechanical properties may change depending on the strain rate of the test. Traditionally, material properties such as the elastic modulus, Poisson's ratio, yield strength, and ultimate strength are determined by a uniaxial tensile test. However, this test is limited to studying materials in quasi-static conditions at strain rates between 0.001 s^{-1} to 10 s^{-1} . For applications in machining and stamping, or ballistic events such as bullet impacts, shell impacts, and explosions, it is common for the loading conditions to reach strain rates of 100 s^{-1} to $10,000 \text{ s}^{-1}$. In dynamic loading conditions, the mechanical response of materials may diverge from its quasi-static properties with increasing strain rate. A dynamic method of material characterization such as the Split Hopkinson Pressure Bar (SHPB) test is used to study mechanical response of materials at strain rates between 100 s^{-1} and $10,000 \text{ s}^{-1}$ [1].

Due to physical phenomenon such as viscoelasticity, materials may exhibit strain rate dependent behavior. For example, the tensile strength of Al-Al₃Ni composite is shown to increase with increasing strain rate [5]. The data acquired from the SHPB can be used in the Johnson-Cook and Zerilli-Armstrong strength models, which are reasonably accurate methods in studying ballistic phenomenon [6-8]. The Johnson-Cook model showed that strain rates of 10^5 s^{-1} are achieved during initial impact of Rolled Homogenous Armor from a projectile with velocity of 1,616 m/s, but reduce to 10^4 s^{-1} during steady-state penetration [7]. Strain rates up to 10^5 s^{-1} may be achieved with a miniaturized SHPB [1, 9], however,

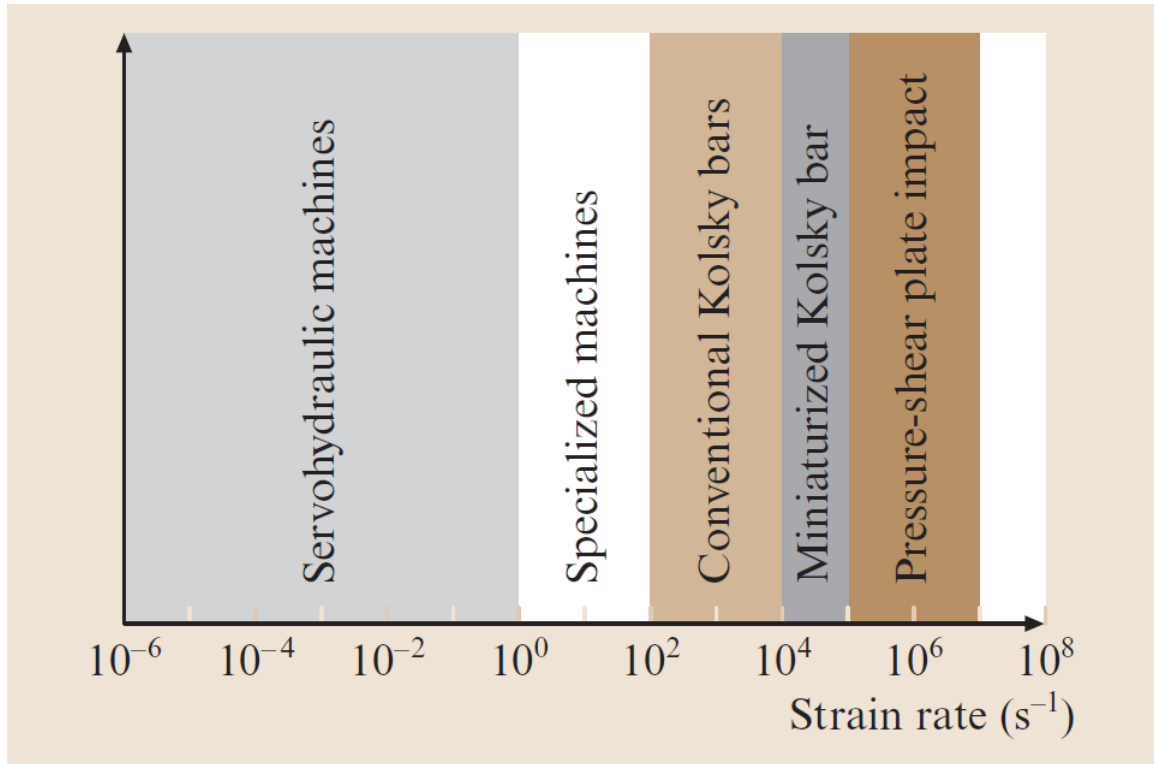


Figure 1.1: Controlled experimental techniques used to study materials at various strain rate regions. Kolsky bars are the general name for a Split Hopkinson Pressure Bar. Reproduced from Ramesh, K.T [1].

anything higher requires explosive plate or light gas gun experiments. The SHPB has also been used to study dynamic material properties of sheet metals at strain rates of 1,000 s⁻¹ to optimize car body structures [10], and for studying rate sensitivity of aluminum alloy sheets also commonly used in car body structures [11]. Figure 1.1 shows the various experimental techniques used to characterize materials over a wide range of strain rates. Uniaxial tensile tests are typically conducted by servo-hydraulic machines which lack the capability of studying dynamic phenomena.

Unlike other high strain rate experiments, the SHPB can provide a robust amount of information about a material's dynamic response, most importantly the material's dynamic stress-strain curve. Other experiments such as a drop tower or an explosive plate provide more qualitative information rather than quantitative [12]. The SHPB experiment

is also robust in the fact that it can be modified for high temperature experiments [13] or different loading regimes: compression, tension, shear, and torsion.

The SHPB requires very careful design in order to produce accurate and repeatable results. The design of the experiment must be modified based on the material being tested. Therefore, it is general practice to design and build a SHPB that is specialized for a particular research area [12]. There are few commercially available test apparatuses, but those that exist come at a significant cost. The commercial test apparatuses are modular by design and can be adapted to fit most testing needs. A commonly used commercial apparatus is manufactured by REL, Inc with a base price of \$100k [14]. The bulk of the thesis will discuss how a relatively inexpensive SHPB can be designed and built to characterize metals, ceramics, composites, and polymers, and will later discuss the outcomes of the design and resulting data.

1.1 – General Description of the Split Hopkinson Pressure Bar

The original SHPB was created to characterize materials in compression. Modifications to the original design can be made to characterize materials in tension, torsion, or shear, however, this thesis will focus on a compressive SHPB. The main components of the SHPB are the striker bar and two compressive pressure bars. A specimen is sandwiched between the two pressure bars. The striker is launched at one end of the pressure bars compressing the specimen. Strain gages are installed on each of the pressure bars to measure the strain waves that result from the experiment. The SHPB theory allows one to determine the specimen's stress-strain curve with the measured strain history of the two pressure bars.

There is no universal design for a SHPB apparatus, however, all designs consist of common design elements which include [9, 11-13, 15]:

- Gas gun or other projectile launching system
- Two long pressure bars of equal diameter
- Linear bearings and pressure bar alignment system
- Momentum Trap
- Strain gages
- Projectile velocity determination
- Data acquisition instrumentation

Most of these elements are seen in Figure 1.2.

The gas gun system consists of a high-pressure reservoir with controls to regulate the pressure of the system. A quick release valve allows the gas to expand and accelerate the striker bar towards the pressure bars. The first pressure bar is called the incident bar and the second pressure bar is called the transmission bar. A velocity measurement system is implemented to measure the velocity of the projectile right before impact. Upon impact, the striker bar produces a compressive pressure wave.

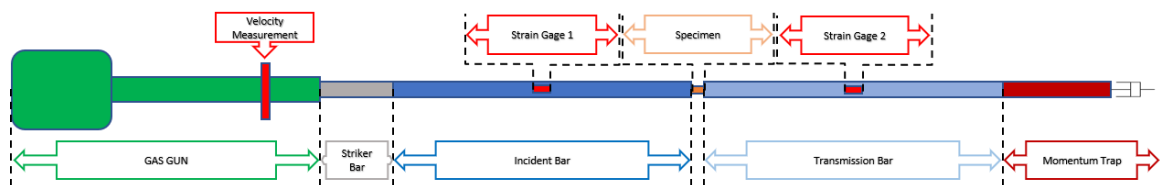


Figure 1.2: General design schematic of a compressive Split Hopkinson Pressure Bar.

The pressure wave propagates along the incident bar and loads the specimen sandwiched between the two pressure bars. A portion of the pressure wave is transmitted

into the transmission bar and also reflected as a tensile wave in the incident bar. The resulting pressure waves are measured using strain gages mounted on the surfaces of the pressure bars. The strain gages are aligned along the center axis of the pressure bars to measure axial strain. In summary, there are three pressure waves: the incident, transmitted, and reflected waves. These pressure waves are used to determine the stress, strain, and strain rate of the specimen. After loading the specimen, the remaining energy in the system is dissipated using a momentum trap.

The maximum stress attainable in a SHPB experiment is dependent on the yield strength of the material selected for the pressure bars; it is general practice to use a high strength steel or nickel alloys such as 4340 or Maraging steel so that high stresses can be attained to deform the specimen. The SHPB experiment is dependent on the assumption of one-dimensional wave propagation, which requires the pressure bars to be sufficiently straight and uniform. The pressure bars are centerless ground to achieve uniform cross-section along their length, as well as, precision straightened to minimize bow in the bars. Bow in the bars will cause bending waves to propagate, which violates this assumption. The pressure bars are supported by a series of linear bearings that allow the pressure bars to slide freely. The bearings are mounted in individual housings, providing a degree of adjustment to align the pressure bars uniaxially. With proper design, the Split Hopkinson Pressure Bar provides robust amounts of data on a material's dynamic response.

1.2 – Historical Aspect

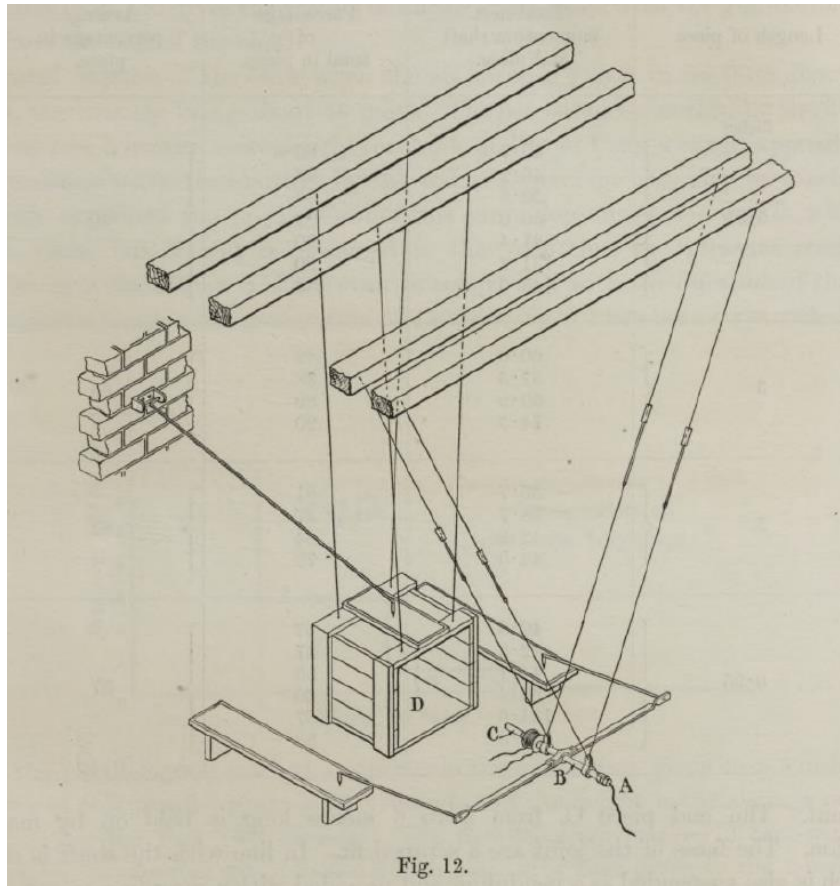


Figure 1.3: B. Hopkinson's original pressure bar experiment. Reproduced from Hopkinson [3].

In 1914, Bertram Hopkinson was interested in studying the pressures generated during the impact of a bullet [3]. Hopkinson derived an experiment involving two rods and a momentum trap: one rod was very long and ballistically suspended; the second rod was wrung together with the first rod and was suspended using an electromagnet. The second rod faced the momentum trap. A schematic of Hopkinson's experiment is seen in Figure 1.3. A bullet was fired at the end of the first rod. A pressure wave was generated from the bullet impact and propagated along the length of the first rod, then transferred its momentum to the second rod. The second rod absorbed the momentum of the first rod, gained velocity, and flew towards the momentum trap. Its momentum was recorded by the

momentum trap. By recording the momentum of the first and second rods, Hopkinson used this data and his derived equations to estimate the pressure of the bullet impact. In 1947, R. M. Davies was the first to consider the use of condenser microphones to measure the time-varying pressure wave, allowing for a more robust analysis of Hopkinson's original experiment [16] .

In 1949, H. Kolsky introduced the idea of splitting the long rod and placing a thin disc of metal in between the two rods to measure stress and strain in the disc [17]. Using Davies idea of using condenser microphones and recording the pressure-time history in the input and output bars, Kolsky derived equations to determine the stress and strain of the thin disc specimen. His design laid the foundations to the modern Split Hopkinson Pressure Bar, and due to his work, the Split Hopkinson Pressure Bar is sometimes referred to as a Kolsky Bar.

1.3 – Current Research

Recently, there has been much interest in investigating materials for military applications. LB Brown et al. used the SHPB system to suggest ways of improving armor designed to stop projectiles [18]. He concluded that the ability to passively strip the metal jacket of the bullet would improve the armor's effectiveness. Meyer et al. used SHPB data and the Johnson-Cook model to model penetration of rolled homogenous armor as well as investigate the penetration of titanium as an alternative lightweight armor [6, 7]. Due to advancements in additive manufacturing technology, researchers have been interested in studying the dynamic behavior of additively manufactured materials [19, 20].

Much research has been conducted to improve the technique to provide more accurate and repeatable results or to expand the scope of the SHPB. Naghdabadi et al.

suggested a method of selecting an appropriate pulse shaper to reduce effects of dispersion. This significantly reduces the trial and error process of selecting a pulse shaper [21]. Similarly, Bagher Shemirani et al. suggested methods of selecting a proper pulse shaper for concrete specimens [22]. Zhong et al. investigates the influence of specimen design in the SHPB test as well as the influence of interfacial friction in the SHPB test [23]. Song et al. suggested a basic standardized SHPB design which offers a platform to build more complex experiments off of [24]. Miao et al. was able to design a SHPB which fixes error due to the tilt effect [25]. To study specimens with low wave impedance, acrylic bars are used. A computational model was created to study viscoelastic wave propagation in PMMA bars [26]. A new method for stress pulse generation has also been investigated using electromagnets [27].

Chapter 2 – THEORY

2.1 – Theory of the Split-Hopkinson Pressure Bar

To derive the relationship between the specimen stress-strain and the pressure bar strains, it is necessary to understand the generation and propagation of the stress wave. A simple approach to understand this is analyzing a perfectly elastic bar impacting a rigid wall as in Figure 2.1. Assume the bar has a length L and bar wave speed c , defined by:

$$c = \sqrt{\frac{E}{\rho}} \quad (1)$$

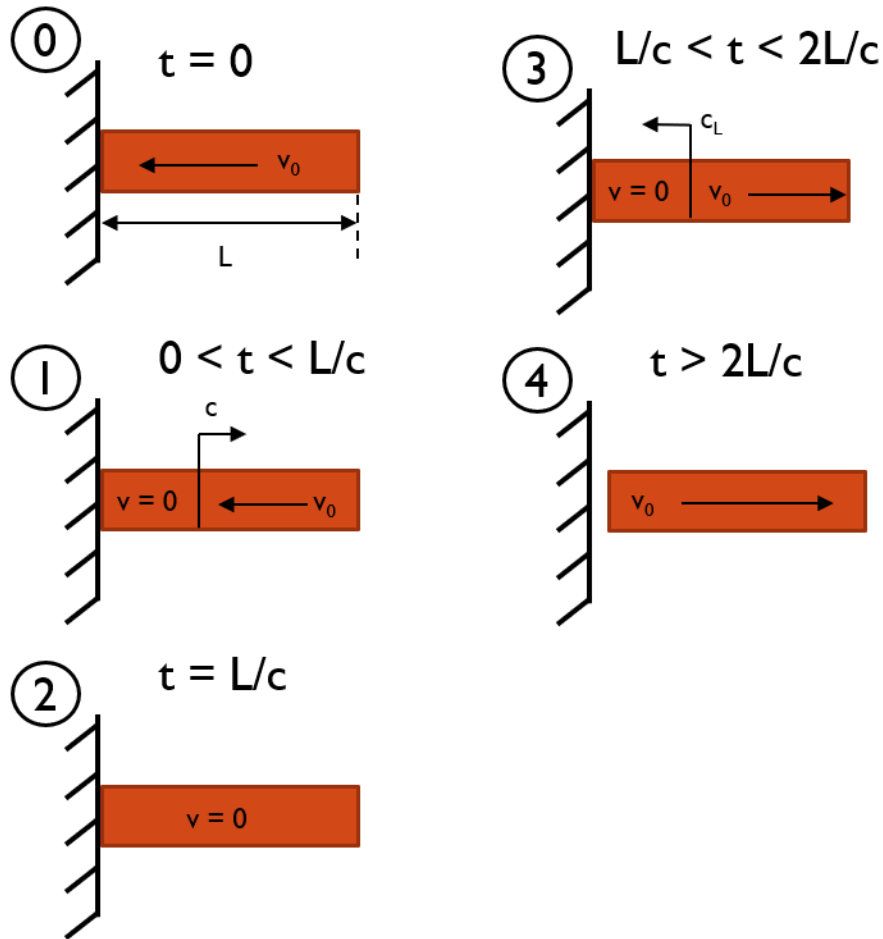


Figure 2.1: Wave propagation of an elastic rod impacting a rigid wall.

where E and ρ are the elastic modulus and density of the bar material respectively [1, 28]. The time for the wave to propagate two full bar lengths is the characteristic time defined by:

$$t = 2L/c \quad (2)$$

At initial impact, when time $t = 0$, the bar is moving with a velocity, v_0 . At time $0 < t < L/c$, a compressive stress wave is generated at the bar-wall interface and begins propagating along the length of the bar as in Figure 2.1 section 1. The bar material behind the wave front comes to rest, while the bar material in front of the wave front maintains its initial velocity. The kinetic energy associated with the material behind the wave front has been transformed into strain energy. At $t = L/c$, the bar has zero velocity; its kinetic energy has been transformed into strain energy as in Figure 2.1 section 2. At $L/c < t < 2L/c$, the compressive stress wave is reflected at the free end of the bar as a tensile stress wave that begins unloading the bar. The material behind the wave front accelerates to the initial bar velocity away from the wall as in Figure 2.1 section 3. At $t > 2L_{st}/c$, the bar releases from the wall with its initial velocity away from the wall [29]. The total loading duration of the bar is the characteristic time $2L_{st}/c$.

When the striker impacts the end of the incident bar, it loads the incident bar for the same duration as if it were a rigid wall. Assuming perfect elasticity and matching wave impedance of the striker and incident bars, all of the striker bar's momentum and energy is transferred to the incident bar. The striker bar comes to rest. This results in a compressive incident wave with a wavelength λ , twice the length of the striker bar L_{st} , that propagates along the incident bar. The resulting incident wave's strain amplitude is

$$\varepsilon_I = \frac{1}{2} \frac{v_{st}}{c} \quad (3)$$

where ε_I is the incident strain and v_{st} is the velocity of the striker bar right before impact [9].

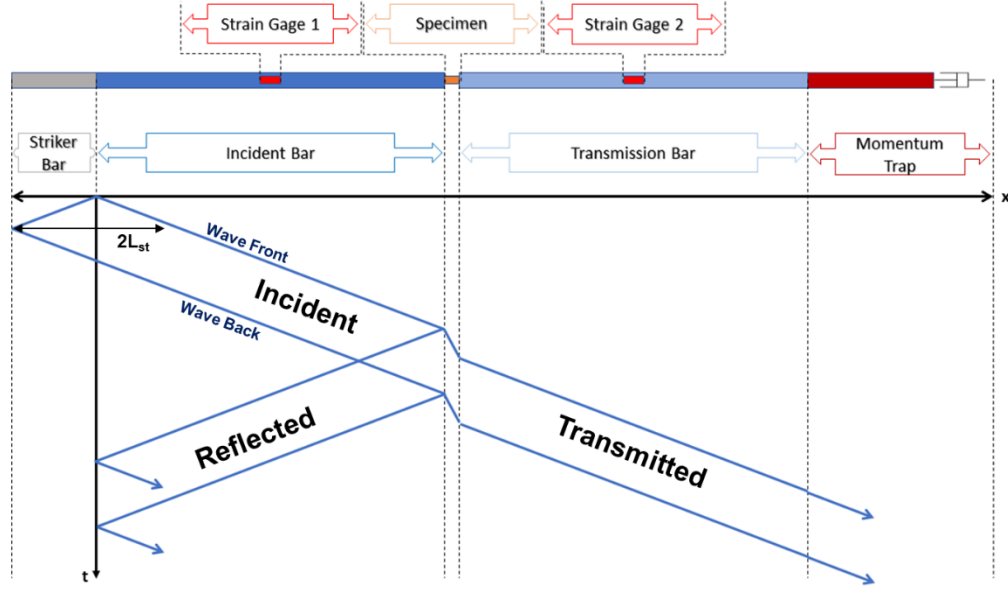


Figure 2.2: Lagrangian diagram for a Split Hopkinson Pressure Bar shows the propagation of the stress wave through time. The x-axis represents position along the SHPB and y-axis represents time.

When the wave propagates, it is assumed that the wave travels in an undispersed manner. Therefore, the wave propagating along the bar is exactly the same at any time t , other than a translation along the bar axis. The incident wave reaches the specimen after $t = L_I/c$, where, L_I , is the length of the incident bar. Due to mismatching wave impedances of the incident bar and specimen, some of the incident wave reflects as a tensile wave along the incident bar; the remaining incident wave is transmitted through the specimen into the transmission bar as a compressive stress wave. When the incident wave transmits through the specimen, several internal reflections occur between the specimen-bar interfaces. These internal reflections can cause issues, however, is generally neglected if the specimen length

is very small compared to wave speed of the specimen material and wavelength of the incident pulse. It is assumed that the stress in the specimen is uniform if the specimen is properly designed. These waves can be visualized through a Lagrangian diagram as in Figure 2.2.

Under these assumptions, equations for stress and strain of the specimen can be derived from the incident, reflected and transmitted strain waves. The bar strains are related to the displacements at the end of the bars as:

$$u_1 = c \int_0^t (\varepsilon_I - \varepsilon_R) dt \quad (4)$$

$$u_2 = c \int_0^t \varepsilon_T dt \quad (5)$$

where, u_1 , is the displacement at the incident bar-specimen interface, u_2 , is the displacement at the transmission bar-specimen interface, ε_R and ε_T , are the strain histories of the reflected and transmitted pulses respectively. The specimen-bar interfaces are visualized in Figure 2.3. The average strain in the specimen can be calculated by

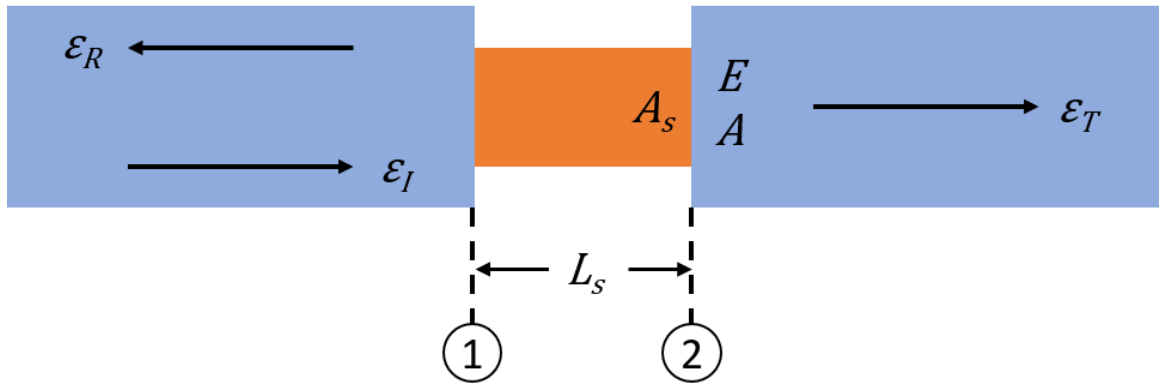


Figure 2.3: Schematic of specimen and strain pulses. 1 indicates incident bar-specimen interface. 2 indicated transmission bar-specimen interface.

$$\varepsilon_s = \frac{u_1 - u_2}{L_s} \quad (6)$$

or, directly by the measured strain histories

$$\varepsilon_s = \frac{c}{L_s} \int_0^t (\varepsilon_I - \varepsilon_R - \varepsilon_T) dt \quad (7)$$

where, ε_s is the specimen strain and, L_s , is the initial length of the specimen. The strain rate in the specimen is calculated by

$$\dot{\varepsilon}_s = \frac{c}{L_s} (\dot{\varepsilon}_I - \dot{\varepsilon}_R - \dot{\varepsilon}_T) \quad (8)$$

The force at each pressure bar-specimen interface is given by:

$$P_1 = EA(\varepsilon_I + \varepsilon_R) \quad (9)$$

$$P_2 = EA\varepsilon_T \quad (10)$$

where, E is the elastic modulus and, A , is the cross-sectional area of the pressure bar. The average stress in the specimen is:

$$\sigma_s = E \frac{A}{2A_s} (\varepsilon_I + \varepsilon_R + \varepsilon_T) \quad (11)$$

where, σ_s is the specimen stress. These equations for stress, strain, and strain rate are referred to as the 3-wave method. If it is assumed that the specimen is in stress equilibrium, $\varepsilon_T = \varepsilon_I + \varepsilon_R$, then the specimen stress, strain, and strain rate history are reduced and expressed as:

$$\sigma_s = E \frac{A}{A_s} \varepsilon_T \quad (12)$$

$$\varepsilon_s = -\frac{2c}{L_s} \int_0^t \varepsilon_R dt \quad (13)$$

$$\dot{\epsilon}_s = -\frac{2c}{L_s} \epsilon_R \quad (14)$$

These simplified equations are referred to as the 1-wave method. Due to Poisson's effect, the cross-section of the specimen changes dynamically during compression. To account for this, corrections to the previous equations for stress, strain, and strain rate are:

$$\sigma = \sigma_s(1 - \epsilon_s) \quad (15)$$

$$\epsilon = -\ln(1 - \epsilon_s) \quad (16)$$

$$\dot{\epsilon} = \frac{\dot{\epsilon}_s}{1 - \epsilon_s} \quad (17)$$

where, σ , ϵ , and $\dot{\epsilon}$ are the true stress, true strain, and true strain rate of the specimen respectively [1].

In practice, the strain waves are measured with linear strain gages. The strain gages are placed far enough from the ends of the bars such that the waves do not overlap. Strain gages act as variable resistors which change resistance with a change in length. This change is reported as the strain gage's gage factor, or GF for short. The GF is directly proportional to the change in resistance as expressed by

$$GF = \frac{\delta R/R}{\delta L/L} = \frac{\delta R/R}{\epsilon} \quad (18)$$

[30]. To measure strain as a voltage, the strain gage is connected in a Wheatstone bridge circuit. The Wheatstone bridge is used to detect very small resistance changes as a result of the change in resistance of the strain gage. The Wheatstone bridge is made up of four resistors: one, two, or four of these resistors are bonded strain gages with the remaining being completion resistors of the same resistance as the strain gage. These are connected

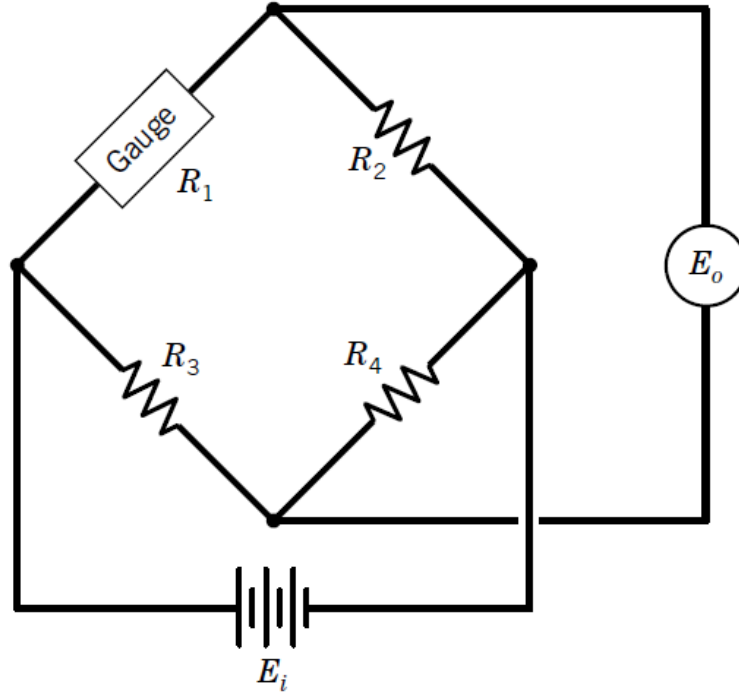


Figure 2.4: Example of a Wheatstone bridge circuit in a quarter bridge configuration.

in a diamond pattern as in Figure 2.4. An excitation voltage, E_i , is applied across opposite legs of the bridge. The completed bridge returns a sense voltage, E_o , recorded by the data acquisition system. When each resistor has the same resistance, then the sense voltage is zero and the bridge is said to be balanced. The Wheatstone bridge can be configured as a quarter, half, or full bridge, each requiring one, two, or four bonded strain gages, respectively. Half and full bridge configurations are used to increase the sensitivity of the strain measurement and to compensate for apparent strains due to temperature, bending strain, or shear [30]. In a quarter Wheatstone bridge configuration, the axial strain is given by

$$\varepsilon = \frac{4 E_o / E_i}{GF(1 + 2 E_o / E_i)} * \left(1 + \frac{R_l}{R_g} \right) \quad (19)$$

where, $\left(1 + \frac{R_l}{R_g}\right)$, corrects for the wire lead resistance to the strain gage, where, R_l is the lead wire resistance, and R_g is the strain gage resistance [30, 31].

For the application of a compressive SHPB, it is required that axial strain be measured. It is common to use half and full bridge configurations to correct for bending waves which propagate due to error in the straightness of the bars. Using one of these compared to the quarter bridge configuration will also increase the sensitivity of the system.

Chapter 3 – EXPERIMENTAL DESIGN AND SETUP

3.1 – Design of Split Hopkinson Pressure Bar

3.1.1 - Striker Launching System

There are several methods of launching the striker bar. Previous work has used explosive detonations, springs, or even hydraulic systems; however, it is most common to use a pneumatic system where a storage of pressurized gas is released to launch the projectile through a tube. Due to its versatility and relatively simple function, a gas gun system was chosen to launch the striker bar.

It is necessary to predict the striker velocity before the experiment is ran for a few reasons. Firstly, a very high striker velocity can potentially yield the expensive pressure bars and break the instrumentation. Secondly, the striker velocity determines the incident strain wave amplitude and is used during calibration. Lastly, the striker velocity is directly proportional to the maximum attainable strain rate during the experiment, which is useful when designing an experiment. The maximum attainable strain rate can be estimated as:

$$\dot{\epsilon} = \frac{v_{st}}{L_s} \quad (20)$$

where, L_s , is the initial length of the specimen [1].

The gas gun system is made up of a barrel, a gas reservoir, a valve, and a system to regulate the reservoir pressure. If it is assumed that the reservoir is large, and that the rate of expansion of the gas is fast compared to the striker, the striker will accelerate by a constant pressure. By applying Newton's 2nd law, an analytical solution for final striker velocity can be derived as:

$$v_{st} = \sqrt{\frac{2lP_{res}A_{st}}{m_{st}}} \quad (21)$$

where, l , is the length of the barrel, P_{res} , is the initial pressure of the reservoir, A_{st} , is the cross-sectional area of the striker, and, m_{st} , is the mass of the striker. This equation assumes effects of friction and compressibility are negligible.

A more representative model of the striker launching can be created. Rahner discussed a numerical model for predicting projectile velocity of a light gas gun system in 2014 [32]. By Newton's 2nd law, acceleration of the striker is dependent on mass, cross-sectional area, and pressure written as:

$$a_{st} = \frac{PA_{st}}{m_{st}} \quad (22)$$

where, a_{st} , is the acceleration of the striker, and, P , is the driving pressure. It is assumed that the reservoir is a straight tube of infinite length and has the same cross-section as the striker. This is so that reflection and refraction waves can be ignored during gas expansion.

Under that assumption, the propelling pressure can be written as:

$$P_p = P_0 \left[1 - \frac{(\gamma - 1)v_{st}}{2c_0} \right]^{\frac{2\gamma}{\gamma - 1}} \quad (23)$$

where, P_p , is the propelling pressure, P_0 , is the initial pressure, $\gamma = \frac{c_p}{c_v}$, is the ratio of specific heats of the propelling gas, and, c_0 , is the speed of sound of the propelling gas [33].

Other factors can be considered as well such as the compressibility in front of the striker.

Back pressure due to compressibility can be described by:

$$\frac{P_b}{P_1} \approx 1 + \left(\frac{v_{st}}{c_1}\right)^2 \frac{\gamma_1(\gamma_1 + 1)}{4} + \frac{\gamma_1 v_{st}}{c_1} \left[1 + \left(\frac{\gamma_1 + 1}{4}\right)^2 \left(\frac{v_{st}}{c_1}\right)^2 \right]^{1/2} \quad (24)$$

where, P_b , is the back pressure, P_1 , is the initial pressure in front of the striker, γ_1 , is the ratio of specific heats of the gas in front of the striker, and, c_1 , is the speed of sound of the gas in front of the striker [33]. Lastly, the pressure loss due to volume increase of the reservoir as the striker moves is

$$P_l = P_0 \frac{\Delta V}{V_0} \quad (25)$$

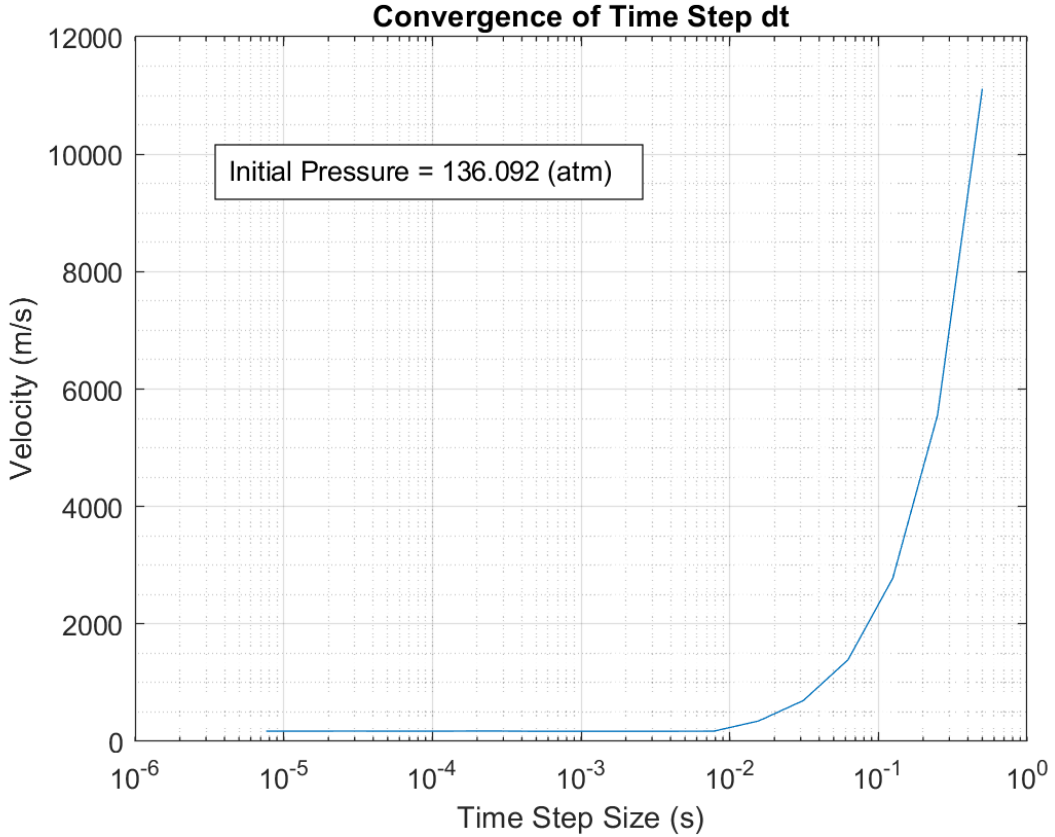


Figure 3.1: Time step convergence of the gas gun numerical model. The time step is chosen such that, $v_{i+1} - v_i < 0.01 \text{ m/s}$. Convergence study shows that a maximum time step of $7.5 \mu\text{s}$ should be used.

where, P_i , is the pressure loss, and, ΔV and V_0 , are the change in volume and initial volume of the reservoir respectively. Using an iterative scheme with short time steps, equations 23-25 may be plugged into equation 22 such that $P(t) = P_p - P_b - P_l$, to calculate the striker acceleration, velocity, and displacement [32-35].

A time step convergence study was performed to determine the maximum time step to be used in the striker launch model. The model ran with decreasing time steps until the cutoff condition, $v_{i+1} - v_i < 0.01 \frac{m}{s}$, was met. The maximum system pressure of 136 atm was used during the simulation. The time step at the cutoff condition was 7.4 μs . Therefore,

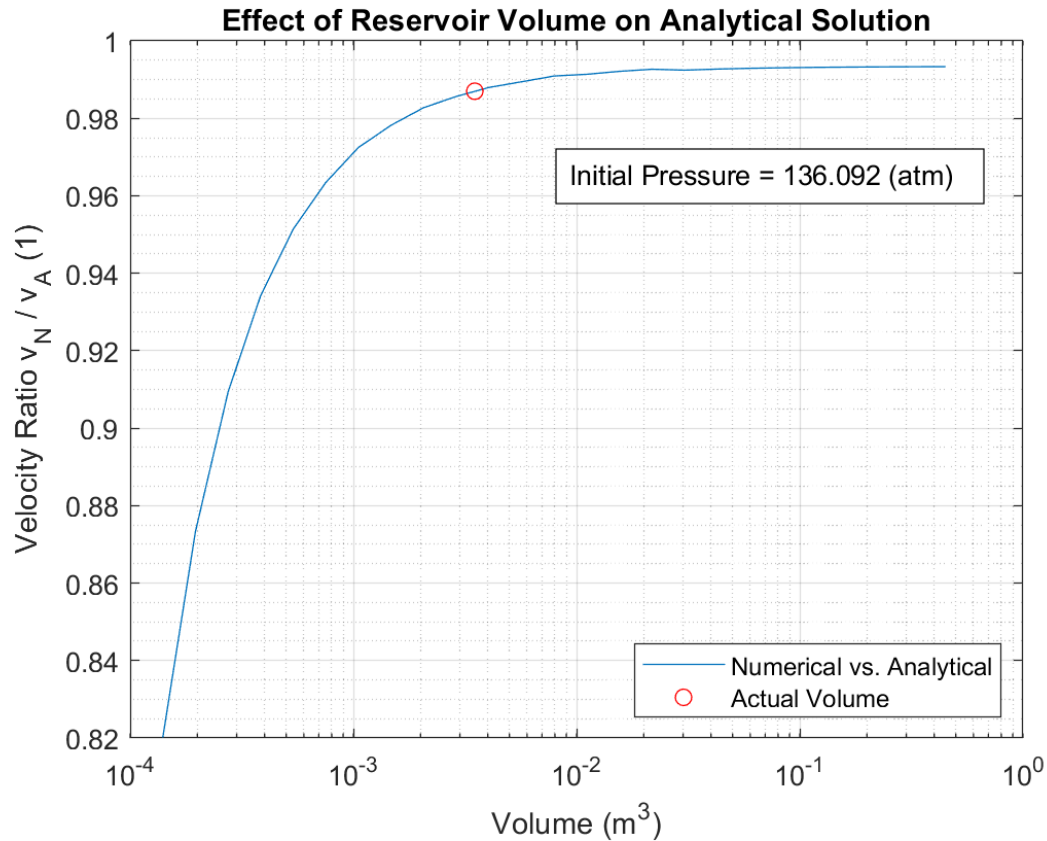


Figure 3.2: Convergence of analytical solution to numerical solution with varying reservoir volume at initial pressure of 136 atm. The red circle indicates the reservoir volume that is used in the design, 0.0035 m³. The analytical solution overestimates the velocity by 1.25%.

the time step should be $7.4 \mu\text{s}$ or less. A time step of $5 \mu\text{s}$ will be used here on out to simplify the time series. The convergence of the time step is seen in Figure 3.1.

The analytical solution for striker velocity is not dependent on volume since it was assumed that the control volume was large. Comparing the analytical solution to the numerical model, it is possible to determine the reservoir volume required for that assumption to be valid. Figure 3.2 shows the velocity ratio between the numerical and analytical solutions, v_N/v_A , changing as a function of volume. The closer this ratio is to 1, the more valid the assumption is. As the reservoir volume increases, the velocity ratio approaches a value of approximately 0.995. A control volume of 0.0035 m^3 has a velocity ratio of approximately 0.987 indicating that the final striker velocities predicted by the analytical solution and numerical model are within 1.3% of each other. The reservoir chosen for the design is seen in Figure 3.3. The reservoir has a volume of 0.0035 m^3 and a rated pressure of 136 atm.

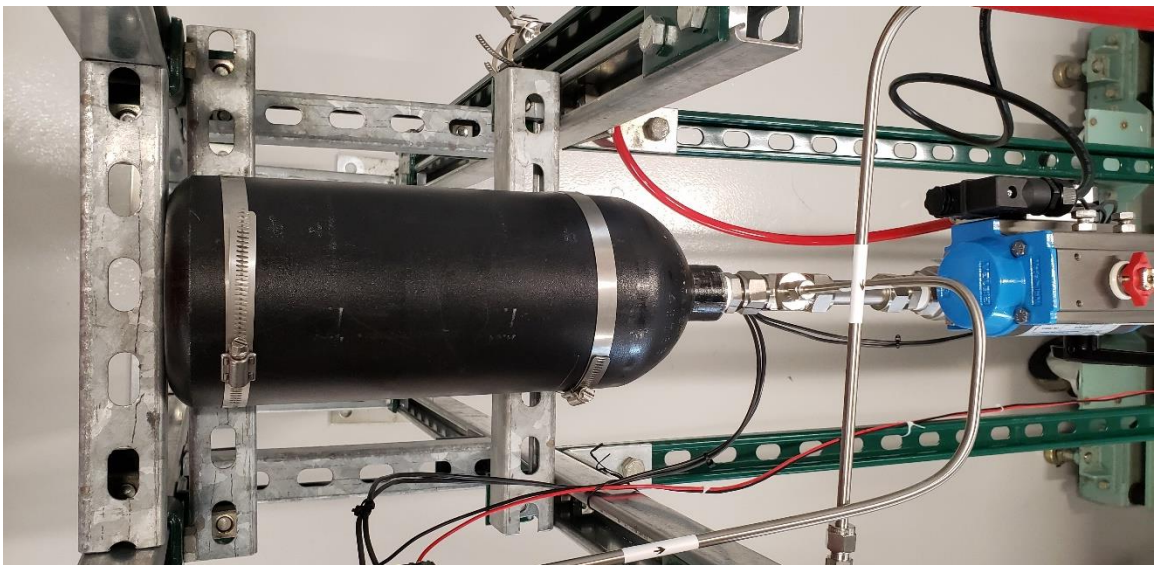


Figure 3.3: Reservoir tank of the striker propelling system. Control volume is 0.0035 m^3 .

The barrel is designed to guide the striker towards the incident bar as it accelerates.

The total length of the barrel is 915 mm. The barrel features two 76 mm exhaust slits

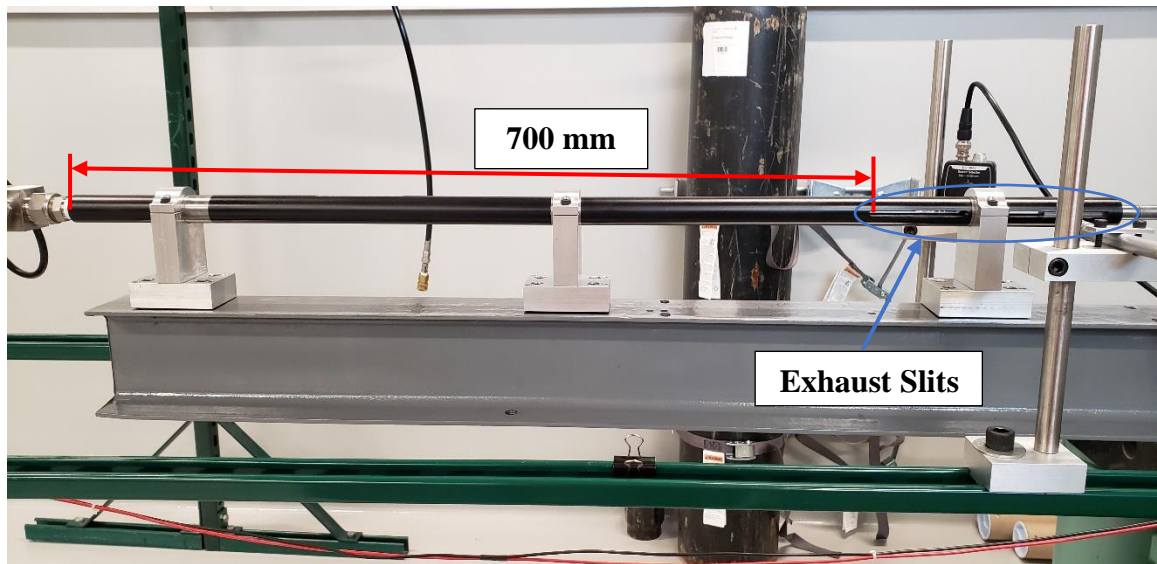


Figure 3.4: Barrel of the SHPB launching system. Two 76 mm slits are machined towards the exhaust end of the barrel. The barrel is held down by three adjustable stage clamps.

machined on one end. The exhaust slits allow propelling gas to escape before the striker reaches the end of the barrel. This helps the striker come to a constant velocity before a velocity measurement is taken. The effective acceleration length for the striker is 700 mm which is the distance from the end of the barrel to the first exhaust slit seen in Figure 3.4. The internal bore is 12.7 mm -0.000 mm to +0.0013 mm, creating a very close fit to the striker. The tolerance on the bore is important to prevent gas from expanding around the striker, which would reduce the propelling force. The barrel is supported by three clamps. The clamps have adjustable stages allowing free alignment of the barrel to the pressure bars.

When preparing for a test, the initial reservoir pressure is set such that a desired striker velocity is achieved. For an acceleration length of 700 mm, reservoir volume of 0.0035 m^3 , and striker mass of 0.078 kg, the striker velocity vs. initial reservoir pressure

curves are shown in Figure 3.5. Both solutions from the numerical model and analytical solution are shown. As the final velocity of the striker increases the numerical and analytical solutions begin to diverge from each other. This is because the numerical model factors in pressure losses and back pressure which oppose the propelling force. The maximum potential velocity for the designed setup is 175 m/s. In practice, this velocity will never be used as it will yield the pressure bars and destroy the instrumentation. The 136 atm capacity of the system is implemented such that strikers of larger masses may be used and still achieve practical velocities of 30 to 50 m/s.

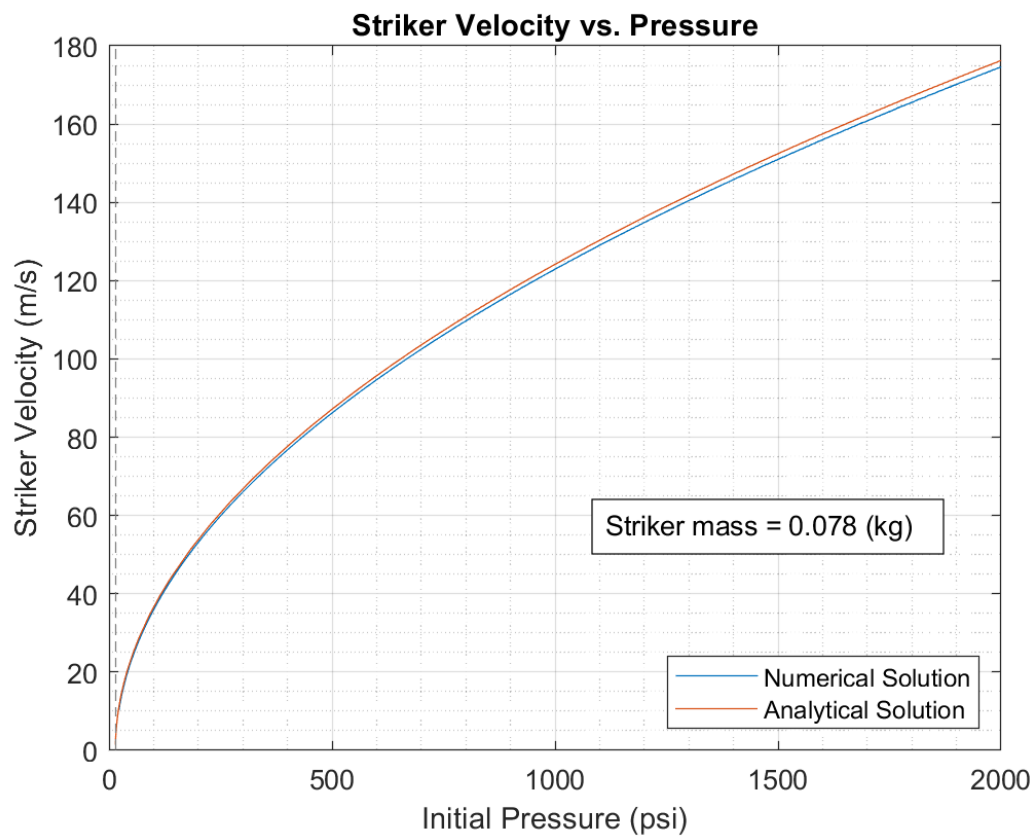


Figure 3.5: Striker velocity as a function of initial reservoir pressure with numerical and analytical solutions. For lower pressures, the analytical solution may be used to accurately predict velocity.

During operation, the compressed nitrogen gas or air is supplied from a large gas cylinder. The control panel controls the flow of the gas into the reservoir. The gas passes through a regulator allowing control of the initial reservoir pressure from 0 to 136 atm. A pressure gauge is connected to the inlet and outlet of the regulator to monitor inlet and outlet pressure. A second redundant pressure gauge is connected to the inlet of the pressure reservoir which is separated from the regulator by a ball valve. The ball valve is used to close off the reservoir from the supply pressure. Another ball valve is fitted to drain pressure from the system. A calibrated blow-off valve is connected to the inlet side of the regulator and releases pressure at 136 atm to prevent over pressurization of the system. The control panel is seen in Figure 3.6.

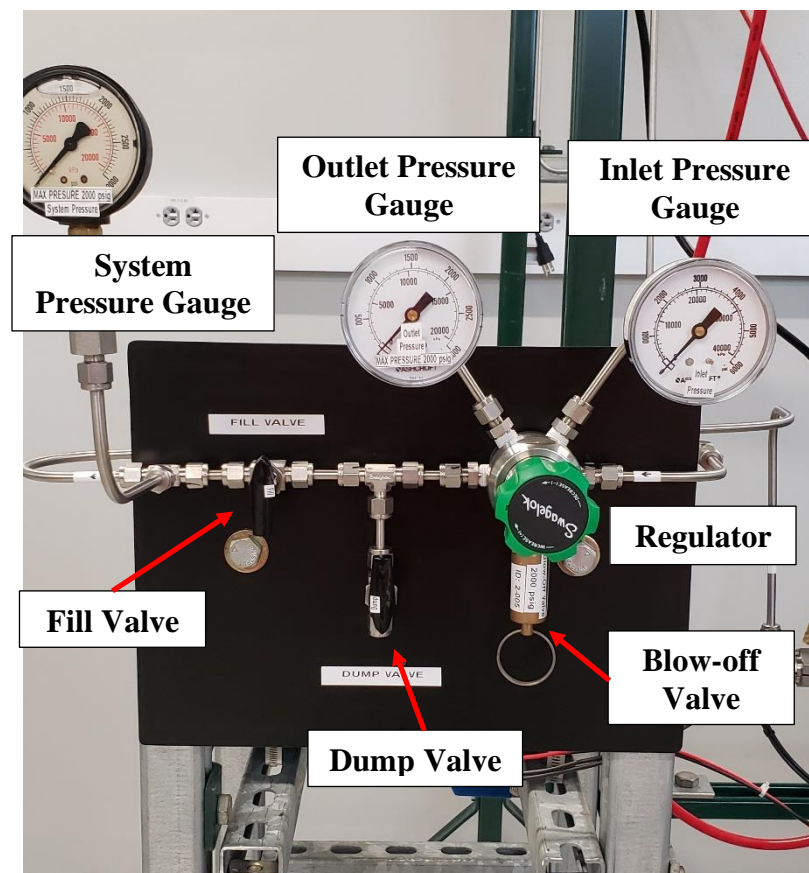


Figure 3.6: Pneumatic control panel to control the initial reservoir pressure.

The launch of the striker is controlled by a pneumatic ball valve. It is important that the expanding gas is unobstructed as it expands. Any change in cross-section or bend in the path will result in a pressure drop and reduce the launch potential of the system. Therefore, the release valve and tubes leading up to the barrel are designed to be straight and have the same cross-sectional area throughout. The release valve is a pneumatic ball valve that can be opened and closed within several milliseconds and is controlled by a solenoid valve. The control software for the SHPB sends a signal to a relay, which opens the solenoid valve, which then opens the release valve. A safety shut off valve is connected in front of the release valve to prevent an accidental launch. The release valve and safety valve are seen in Figure 3.7.

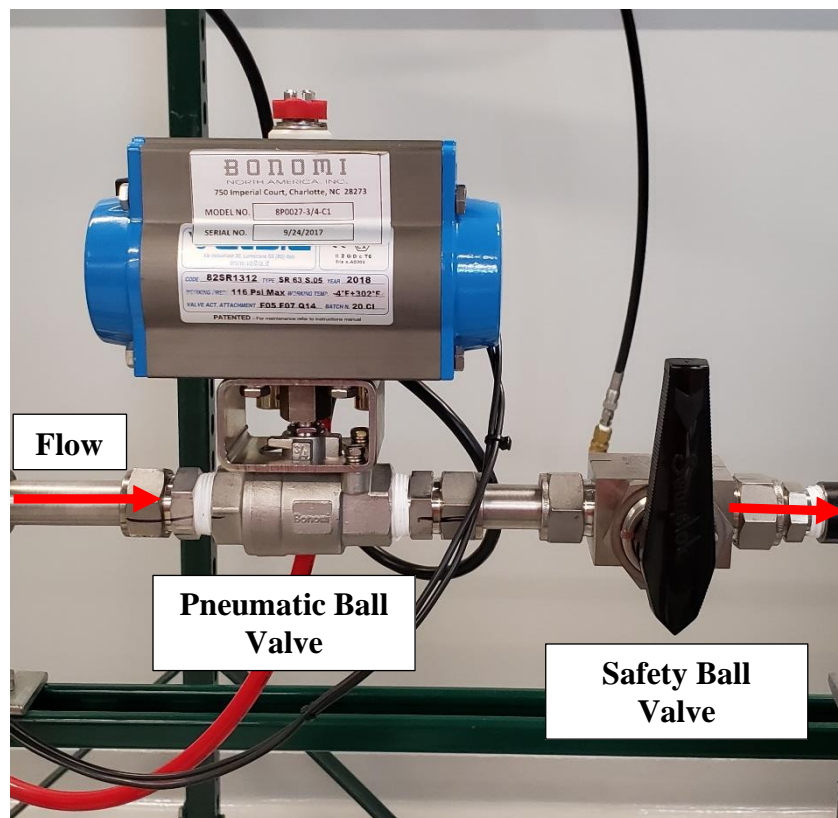


Figure 3.7: Release valve and manual safety shut-off valve.

3.1.2 - Pressure Bars

The pressure bars are designed such that the strain pulse generated by the striker bar is transmitted uniaxially as a uniform stress wave. The bars must be strong enough to withstand repeated high velocity impacts from the striker bar. The incident wave can be approximated by a square wave with a duration $2L_{st}/c$ and amplitude $v_{st}/2c$. In practice, the incident wave is comprised of many frequencies taken to be integer multiples of the dominant frequency [36]. The dominant frequency is defined by

$$\omega_0 = \frac{2\pi}{T} \quad (26)$$

where, ω_0 , is the dominant frequency, and, T , is the period of the pulse defined by $T = \frac{2L_{st}}{c}$ [16, 36]. One of the fundamental assumptions of the SHPB analysis is that the pressure waves propagate in an undispersed manner. The phase velocity, c_p , of a particular frequency is given by the relation

$$c_p = \frac{\omega}{2\pi} \Lambda \quad (27)$$

where, Λ , is the wave length [36]. The dispersion relation relates the diameter of the bar, d , to the phase velocity. For relatively large wavelengths, this can be estimated with the Raleigh approximation

$$\frac{c_p}{c_0} = 1 - \nu^2 \pi^2 \left(\frac{d}{2\Lambda} \right)^2 \quad (28)$$

where, ν , is the Poisson's ratio of the bar material. The Raleigh approximation shows that the dispersion of longitudinal waves along the bar is a function of $\frac{d}{2\Lambda}$. It has been shown that this ratio, when greater than 0.1, will result in nonuniform stress distribution greater

than 5% across the cross-section of the bar [16, 36]. If the ratio is greater than 0.1, a strain gage measurement on the surface of the bar will not represent the strain across the entire cross-section of the bar. It is common for pressure bars to be between 12.7 mm and 25.4 mm in diameter. Bars of larger diameter will exponentially increase the effects of dispersion. Large diameter pressure bars are commonly used when characterizing brittle materials like concrete [37]. For the general application discussed in this thesis, 12.7 mm diameter bars are chosen which minimize nonuniform stress distribution.

To promote uniaxial wave propagation, the pressure bars must be sufficiently long compared to their diameters. General recommendations suggest an aspect ratio of about 50:1 to ensure uniaxial wave propagation [9, 36, 37]. The pressure bars must also be sufficiently straight. Bars with bow will introduce unwanted bending waves. The bending waves can be eliminated by using a half or full bridge configuration in the Wheatstone bridge design; however, it is best to eliminate the bending waves by manufacturing the pressure bars with precision straightening techniques. The straightness tolerance of the pressure bars is 0.17% or 0.17 millimeters per meter. The nominal lengths of the incident bar and transmission bar are 1250 mm and 580 mm respectively. The pressure bars have aspect ratios of 98.4:1 and 45.7:1 respectively and should promote uniaxial wave propagation.

The bar material is very important; the stress wave produced by the striker must always be less than the yield limit of the bar material. The modulus of elasticity and wave speed of the bar are also important. For testing soft materials, it is necessary to choose a bar material with lower elastic modulus to amplify the signal of the stress waves [9]. For specimens such as rubber, the reflected pulse is almost identical to the incident pulse and

transmits a very weak transmitted pulse. A material such as Al 7075-T6 is commonly used for this application for its lower elastic modulus, but high strength [38]. When testing hard ceramics, the specimen is often equal in strength or stronger than the pressure bar material. In this case, the pressure bars must be made from a very strong material such as C350 Maraging Steel. C350 has a superior yield strength of 2413 MPa. For specimens stronger than C350, the specimen must be designed to reduce the stress in the bars. A specimen with small cross-sectional area will amplify the stress wave, creating enough stress to yield the specimen. This, however, produces a stress concentration at the bar interface which may dent the bar interfaces. To reduce this stress concentration, hard platens can be placed between the specimen and the bar interfaces. These are usually made of hardened tool steel or tungsten carbide. The platen material should have the same wave impedance as the bar material to prevent reflections, which is written as

$$(\rho c A)_{\text{platen}} = (\rho c A)_{\text{bar}} \quad (29)$$

[9].

To test a range of different materials, the SHPB facility is designed with interchangeable pressure bar sets. For testing polymers, metals, and ceramics, a set of pressure bars are made from C350 and another from C300. For testing soft polymers, rubbers, and gels, the pressure bars are made from 7075-T651. The dimensions of the pressure bars are presented in Table 1.

Table 1: Table of pressure bar sets

Bar Material	Bar Diameter (mm)	Incident Bar Length (mm)	Transmission Bar Length (mm)	Nominal Elastic Modulus (GPa)	Nominal Yield Strength (MPa)
C350	12.7	1250	580	200	2363
C300	12.7	1250	580	190	2020
7075-T651	12.7	1250	580	71.7	503

3.1.3 - Strain Gages and Signal Conditioning

When selecting strain gages for a compressive SHPB test, the type of bridge configuration must first be determined. It was discussed that half and full bridge configurations are ideal in theory since they can compensate for bending waves. Error during the installation of the gages must be considered though. If two gages are mounted diametrically, any deviation in the positioning of the two gages will create a phase delay which may produce erroneous results at the edges of the strain pulse. The bending waves should be nearly eliminated by precision manufacturing the pressure bars straight, and by aligning the bars. Therefore, it is simpler to install and potentially more accurate to use a quarter bridge configuration. If needed, the bridge can be expanded to a half or full bridge configuration by adding additional strain gages.

Due to the dynamic nature of the experiment, the frequency response of the strain gage must be examined. Evaluation of the metal foil strain gage determines that the cutoff frequency, f_c , is

$$f_c > 0.35 / \left(\frac{0.8L_g}{c} + 50 * 10^{-9} \right) \quad (30)$$

where, L_g , is the gage length of the strain gage [39-41]. A strain gage mounted to a C-350 bar with gage length of 1.59 mm will have a cutoff frequency of ~1.15 MHz. Since the

strain sensing foil of the strain gage is not in direct contact of the bar surface due to its insulating backing, the backing's effect on the frequency response must also be considered. It was determined that this effect can be ignored if the rise time of the strain pulse is at least 5 times longer than the natural period of the system [39]. The natural period is determined by

$$T_N = 2\pi \sqrt{\rho_f / \left[E_f \left(\frac{\pi}{L_g} \right)^2 + \frac{G_b}{h_b h_f} \right]} \quad (31)$$

where, ρ , E , G , and h , are the density, Young's modulus, shear modulus, and height of the matrix respectively, and the subscripts f and b denote the values of the filament and base film, respectively [39]. The strain gage measures the average strain over its gage length as in Figure 3.8. A smaller strain will measure a high frequency wave more precisely than with a large gage length. To minimize this averaging, the gage length should be small.

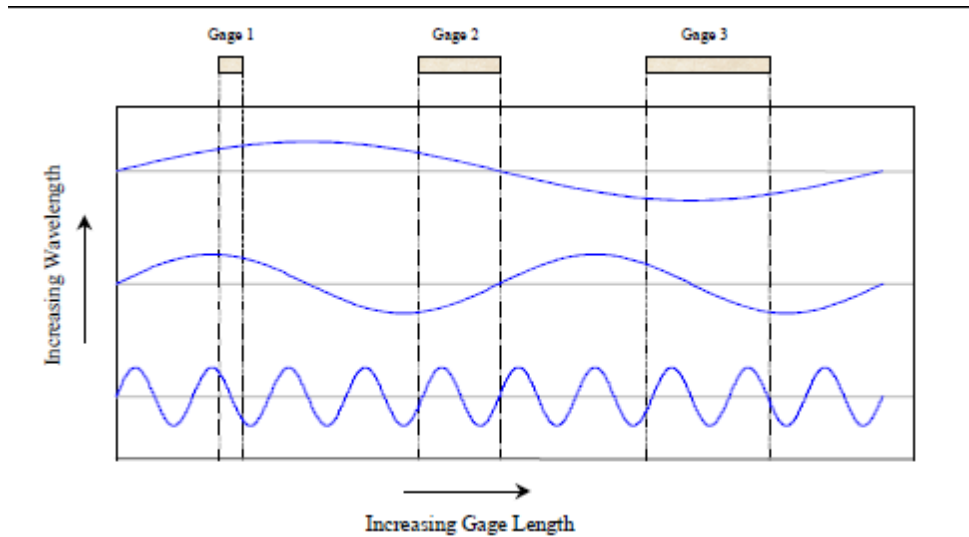


Figure 3.8: The strain gage measures the average strain over its gage length.

In any SHPB test, it is well known that the strain gages can break due to the high acceleration of the strain pulse [15]. Acceleration of the strain gage was estimated to be on

the order of $800,000 \text{ m/s}^2$ [42]. Through experiment, wire connections at the solder tabs are the most common failure mode. Examples of connecting wire failures are seen in Figure 3.9. To reduce inertia, the least amount of solder should be used to attach the lead wire [42]. Similarly, the thinnest lead wire possible should be used. With proper installation, impact velocities as high as 50 m/s are achieved without breaking the strain gages, which improves upon previous work which increased the upper limit of impact velocity to 40 m/s [42].

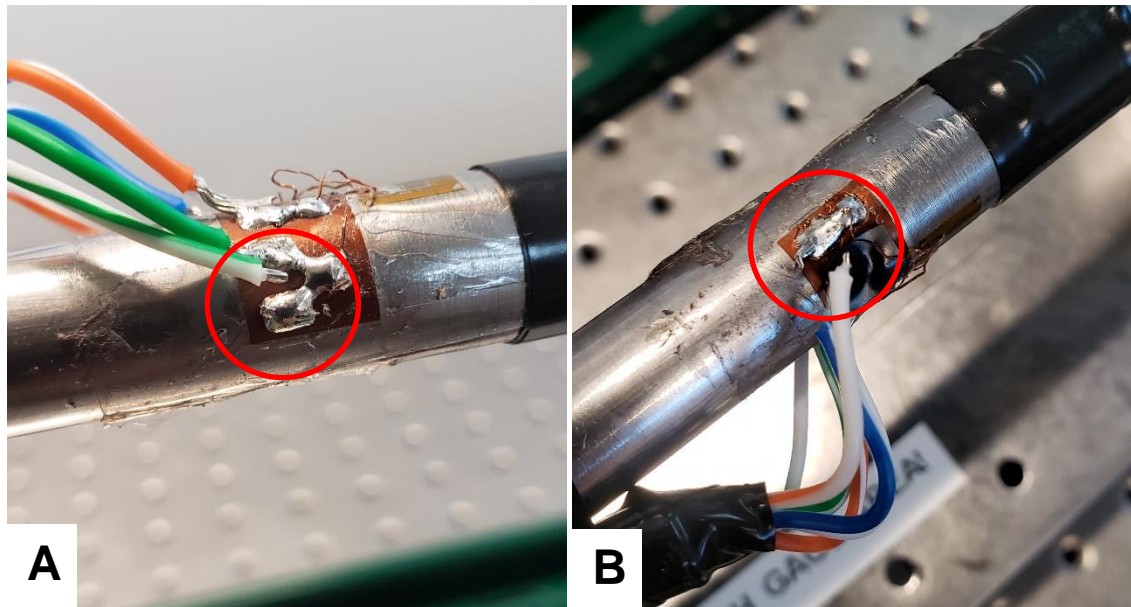


Figure 3.9: Examples of broken connecting wires on incident bar terminal pad. **A.** Broken connecting wire for axial gage. **B.** Broken connecting wire for transverse gage V+ excitation wire.

The strain gage selected is a Micro-Measurements EA-06-062TT-350/L. The gage length is 1.59 mm which results in a high frequency response of ~ 1.15 MHz. This model comes with pre-attached lead wires made of thin copper and uses minimal solder to attach; this minimizes inertia. The model is a Tee rosette which has two strain gages mounted 90 degrees from each other. One of these gages is used to measure the axial wave and the other to measure the transverse wave. Each strain gage rosette requires two Wheatstone bridge completion circuits to measure the axial and transverse waves separately. The GFs of the axial gage and transverse gage are $2.145 \pm 0.5\%$ and $2.115 \pm 0.5\%$ respectively. The strain gage rosette should be bonded at least half the wavelength of the incident pulse from the ends of the pressure bar, but is recommended to be at least one full wavelength away. The strain gage rosette is bonded to the surface of the pressure bars using Micro-Measurements M-Bond AE-10 adhesive, and is bonded far enough from the ends of the pressure bars such that the incident and reflected waves do not interfere.

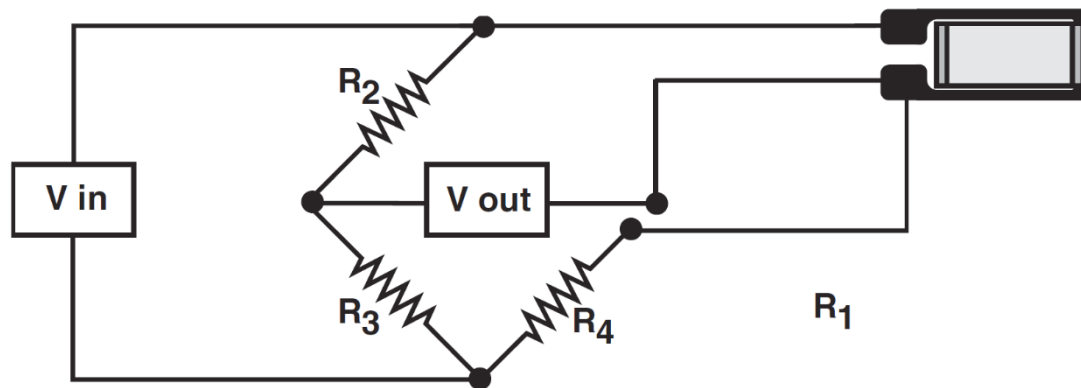


Figure 3.10: Schematic of a 3-wire quarter Wheatstone bridge. Reproduced from Micro-Measurements Application Note VMM-5.

The strain gage rosette is connected to the Wheatstone bridge through a 6 wire twisted pair double-shielded cable to minimize EMF interference. Each gage is connected as a 3-wire connection shown in Figure 3.10. The completion resistors R_2 , R_3 , and R_4 are Riedon 350 Ω precision resistors with 0.01% radial accuracy. These match the resistance of the strain gage such that the bridge is balanced in an unstressed state. The wires and the thin copper lead wires connect at a bonded terminal pad attached to the bar providing strain relief. The lead wires and connecting wires are arched at the terminal pad which provide additional strain relief. The strain gage rosette and terminal pad are seen in Figure 3.11.

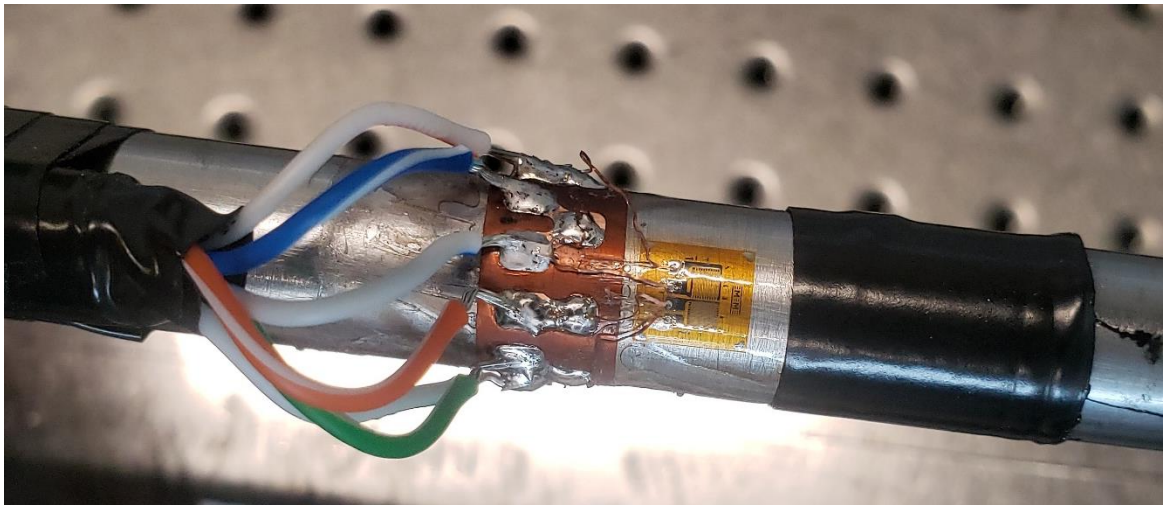


Figure 3.11: Installed strain gage on incident pressure bar.



Figure 3.12: Kulite KSC-2 signal conditioners.

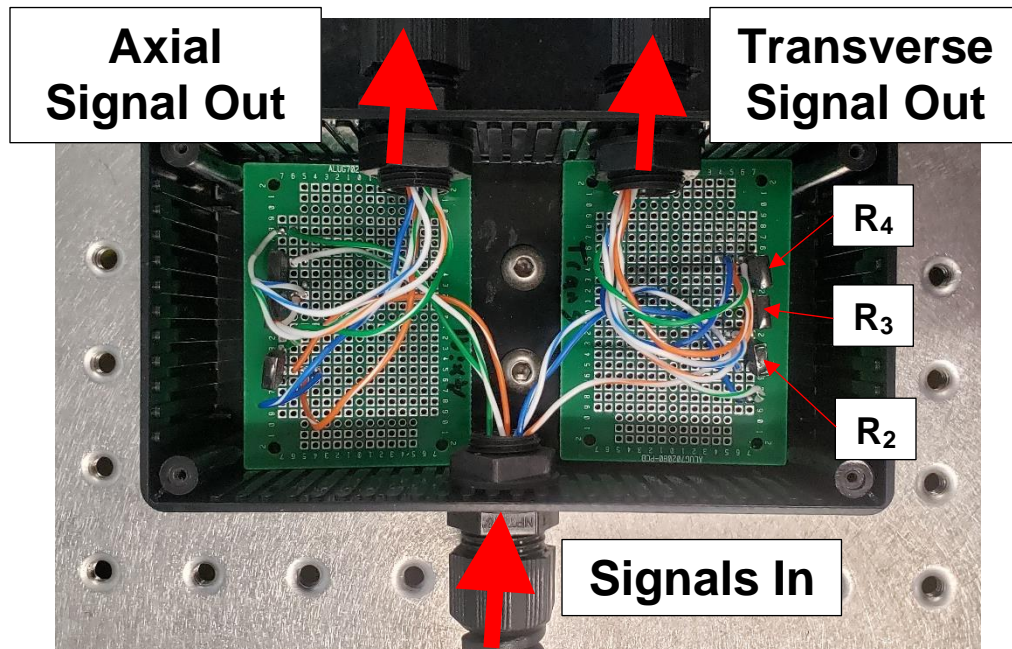


Figure 3.13: Wheatstone bridge completion circuits for axial and transverse measurements.

Due to the low voltage signal produced by the Wheatstone bridge seen in Figure 3.13, it is necessary to pass the analog signal through a signal conditioner before digitizing. To streamline the data acquisition system, the signal conditioner must amplify the signal,

provide excitation voltage to the Wheatstone bridge, and apply an offsetting balance voltage. The most important factor in the signal amplification is the bandwidth. The dominant frequency for the current setup is no greater than 39 kHz. Therefore, the bandwidth of the amplifier should be at least 39 kHz to resolve the wave. For accurate analysis, it is generally recommended that the signal conditioner have a bandwidth of at least 100 kHz [9, 24].

For the current setup, the Kulite KSC-2 signal conditioner, pictured in Figure 3.12, is used. This signal conditioner has a bandwidth of 500 kHz. The KSC-2 provides a bipolar excitation voltage up to 12 V and has an auto balancing feature which can zero the Wheatstone bridge before testing. A 6-pole Bessel filter or 6-pole Butterworth filter may be used for anti-aliasing. Prefilter gain is variable up to 128x and postfilter gain is variable up to 16x.

After passing through the signal conditioner, the analog strain signal needs to be digitized and recorded. For this setup, National Instruments equipment and LabVIEW are

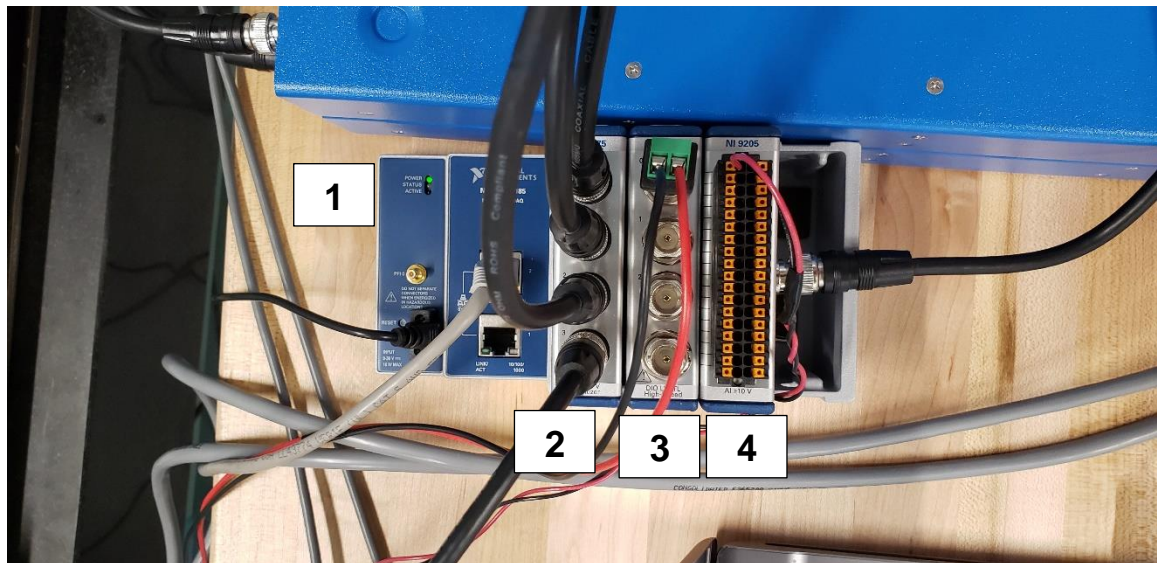


Figure 3.14: 1. National Instruments cDAQ 9185 chassis with 2. NI 9775 digitizer, 3. NI 9402 DIO, and 4. NI 9205 AIO modules.

used. The NI 9775 digitizer can sample at 10 MS/s/ch. The digitizer is seen in Figure 3.14. The high sample rate helps with anti-aliasing and allows a simpler anti-aliasing filter to be used [43].

The striker velocity is measured using a laser and photodiode system. A low powered laser (< 5 mW) passes through the exhaust slits of the barrel. The laser is mounted so that it is perpendicular to the striker's velocity. A photodiode is placed on the opposite side of the barrel, in line with the laser. When the laser beam is broken by the striker, the photodiode responds with a voltage drop. Similarly, when the laser beam is reintroduced after the striker passes, the voltage increases. As the striker bar travels down the barrel, it will break the laser beam for some time, then reintroduce the beam after it passes. The time that it takes for the striker to do this is measured by the photodiode. If the length of the striker is known, it is simple to calculate the velocity of the striker. The velocity measurement is an average of the striker velocity over a period. For the measurement to be accurate, the laser is placed as close to the end of the barrel as possible where the striker will be moving with a constant velocity.

When choosing the photodiode, the rise/fall time and the spectral responsivity must be considered. From the analysis of the striker velocity, the expected maximum velocity is 175 m/s. In practice, the striker should never reach this velocity, but will be used to design a robust velocity measurement system. For a 76.2 mm striker travelling at 175 m/s, the characteristic time is 435 μ s. To measure this velocity with an accuracy of 0.1%, the rise/fall time of the photodiode needs to be less than 435 ns. The photodiode should be as sensitive as possible to the wavelength of laser being used. The laser used has a wavelength of ~ 650 nm. The Thorlabs DET36A2 bias detector has a rise time of 14 ns and responsivity

of 3.4 A/W at 650 nm, which is suitable for this application. The photodiode voltage output is recorded by the NI 9205 analog input module seen in Figure 3.14.

3.1.4 - Bar Alignment

The striker, incident, and transmission bars must be in good alignment to promote uniaxial wave propagation. If the incident and transmission bars are slightly misaligned, a wave impedance mismatch at the bar interface will result in energy loss and undesired reflections. If the bars are in good alignment, the wave will propagate through the bar interface undisturbed with little energy loss. Good alignment is most evident when comparing the incident, reflected, and transmitted waves of a test with no specimen and the bars in contact; the incident and transmitted waves will match, and the reflected wave will be negligible. An example of good axial alignment is seen in Figure 3.15.

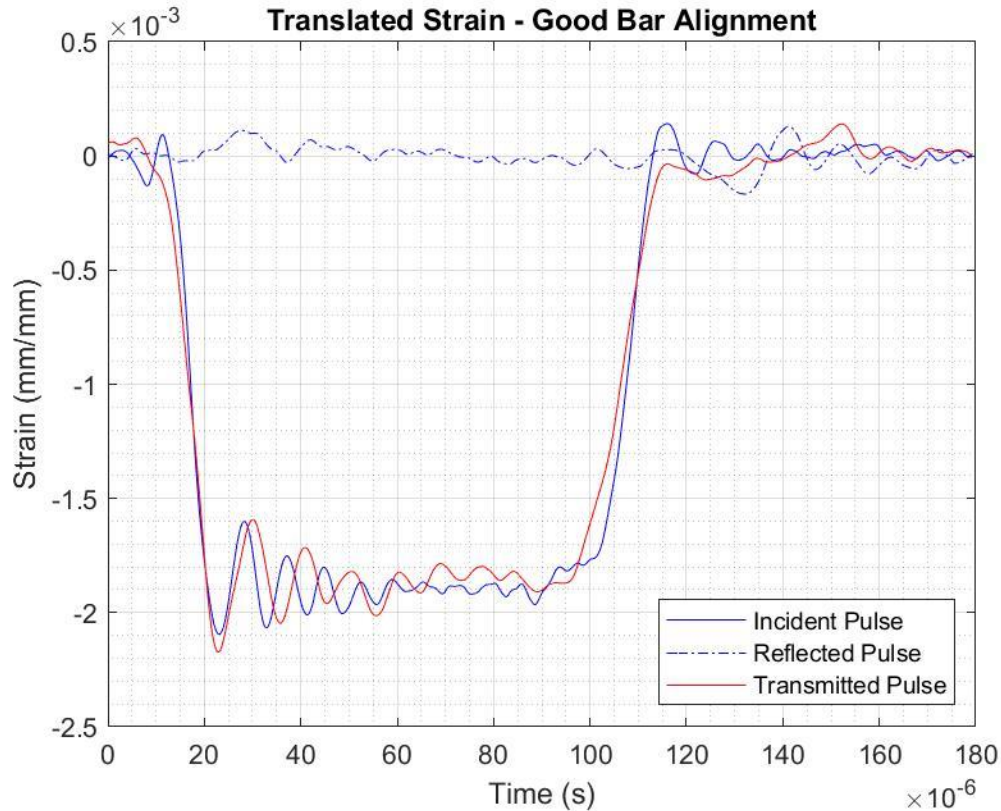


Figure 3.15: Good axial alignment of pressure bars. Incident and transmitted pulses match and the reflected pulse is close to zero.

Bar alignment is achieved through a series of linear bearings mounted in pillow blocks. Song et al. used a series of Frelon[®] - coated linear bearings mounted in pillow blocks to achieve good axial alignment [24]. The pillow blocks are designed to be adjusted with an adjustable stage. Each pillow block stage has four set screws allowing the linear bearing inside to be aligned with the other linear bearings. When the bearings are well aligned, the pillow blocks are secured to the base. The pillow blocks feature caps which hold the linear bearings in place. Removing the caps allow the bars to be removed and replaced without losing alignment. The bearing selected is a ceramic lined Al 6061 fixed alignment sleeve bearing. The bearing has an oil port which allows oil to form a thin film between the bar and bearing surface. The pillow block and bearing are shown in Figure

3.16. The bars are supported by the bearings every 330.2 mm. The incident pressure bar is supported by four bearings; the transmission and momentum trap bars are supported by two bearings each.

After securing the pillow blocks and bearings to the base, the bar alignment can be checked with a laser alignment system as in Figure 3.17. The bars are in good alignment when the laser can pass through a small pinhole in every bearing in the series.

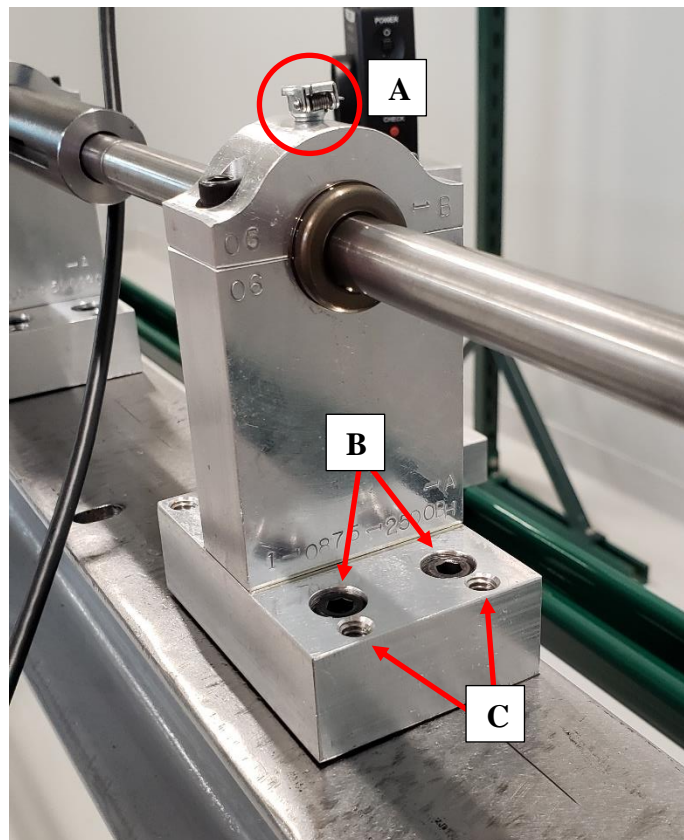


Figure 3.16: Ceramic lined linear bearing mounted in split pillow block bearing housing. The pillow block housing uses four set screws to adjust the alignment of the bearing. **A.** Oil port. **B.** Mounting screws. **C.** Adjustment set screws

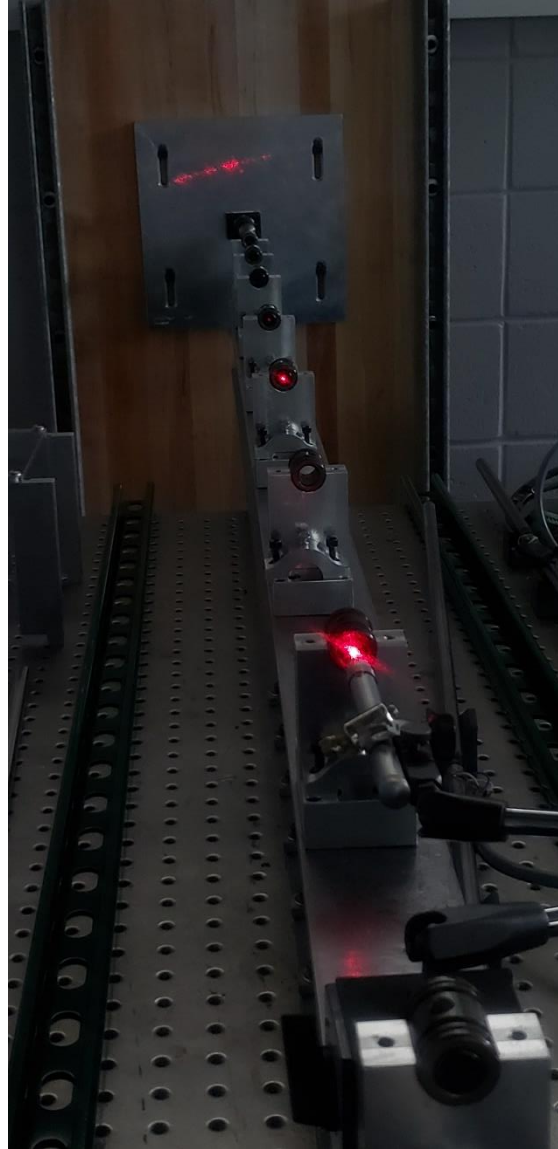


Figure 3.17: Laser alignment of bearings.

3.1.5 - Momentum Trap

A momentum trap is deployed at the end of the transmission bar to dampen the remaining momentum in the system. Without a momentum trap, the stress waves would continue to propagate in the system, loading the specimen many more times; this is undesirable behavior. The momentum trap consists of a bar made of the same material as the pressure bars, and a shock absorber as in Figure 3.18. When a strain pulse reaches the end of the transmission bar, its energy and momentum is captured by the momentum trap



Figure 3.18: The momentum trap consists of a bar and shock absorber.

bar, instead of reflecting at the end of the transmission bar. The momentum trap bar pushes into a shock absorber which absorbs the momentum. The shock absorber has an energy capacity of 209 J over a stroke length of 23 mm. The momentum trap is mounted to a heavy structure isolated from the system to avoid shocking the system.

3.1.6 – Structure

The structure supports each subsystem, most importantly, the pillow blocks holding the pressure bars. The structure should be heavy and rigid similar to the optical table in [24]. Other SHPBs are mounted on large I-beams as is [9]. The structure used in this work is a steel I-beam. The pillow blocks are aligned and mounted on the I-beam by threaded

holes which are machined into the I-beam. To add mass to the structure, the I-beam is bolted to a breadboard which sits on a granite surface plate. The total length of the I-beam is 3.05 meters. A U-channel structure supports the gas gun system.

3.2 – Specimen Design

The specimen must be properly designed to perform a valid SHPB test. Generally, the specimen is a solid cylinder with flat and parallel faces; however, other specimen shapes may be used after special consideration. Two common design considerations are radial inertia and interfacial friction. Davies and Hunter concluded that the optimal specimen geometry to minimize radial inertia and interfacial friction is

$$\frac{d_s}{L_s} = \frac{4}{\sqrt{3}} \quad (32)$$

where, d_s , is the specimen diameter [29, 44]. The specimen should be fully engaged with the pressure bars through the entire loading cycle. Most materials will expand radially during compression, so the final diameter of the specimen should be less than the bar diameter. Before testing, the specimen interfaces should be lubricated to minimize interfacial friction that was shown to increase the nonuniformity of stress and strain in the specimen as seen in Figure 3.19 [4, 23]. As the coefficient of friction between the bar and specimen increases, the specimen becomes more constrained at the interface, resulting in a drum shaped deformation. Friction causes a multiaxial stress distribution in the specimen, violating the uniaxial loading assumption. Friction at the interfaces with a friction coefficient of $\mu = 0.2$ was shown to reduce the reflected pulse by 11% and increase the transmitted pulse by 10%, resulting in inaccurate stress analysis [23]. For general testing, petroleum jelly is used as an interfacial lubricant.

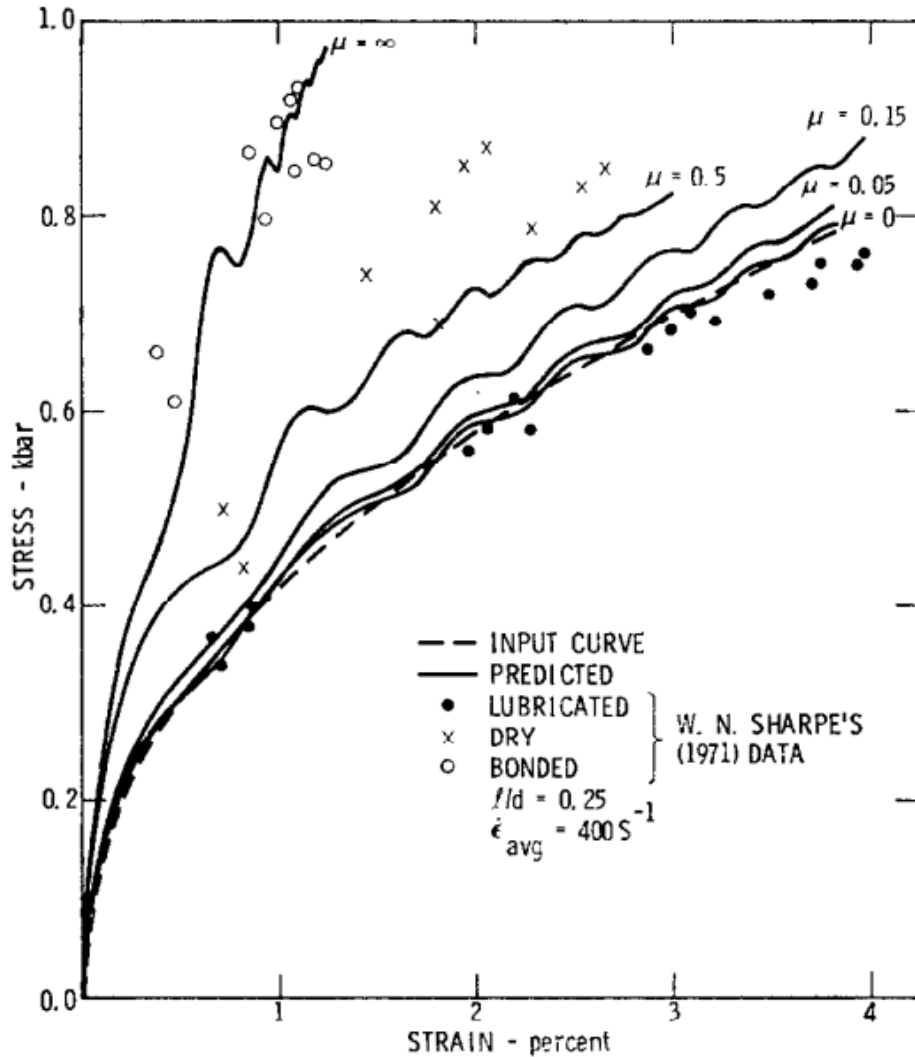


Figure 3.19: Comparison of calculated response curves of bonded, dry, and lubricated specimens. Increasing the coefficient of friction significantly increases the stress in the specimen. Reproduced from Bertholf and Karnes [4].

An important assumption of the SHPB is that the specimen is in full contact with the ends of the pressure bars. If there is any deviation in the flatness and parallelism of the faces, uneven loading of the specimen will occur due to the tilt effect [25].

3.3 – Data Processing

The raw data is processed through a MATLAB script, which ultimately outputs a stress-strain curve. The test parameters including pressure bar parameters, specimen

parameters, and amplifier settings are imported from a master test log. The strain gage voltages are converted into strains and normalized by the amplifier gain settings. The data is smoothed using a Savitzky-Golay filter to remove noise. The most important step in the data processing is determining the starts of the incident, reflected, and transmitted waves. An algorithm is implemented which approximates this. The algorithm takes a time derivative of the incident bar strain-time history, then looks for where the derivative decreases below a certain threshold, marking the index. It then looks at the strain ahead of this index to determine if it is in fact a strain wave. If both conditions are met, the algorithm will mark the index as the start of the incident pulse. The algorithm approximates the start of the incident wave, so manual adjustment of may be required. The reflected pulse and transmitted pulse start times are determined by calculating the transit time of a strain wave between the strain gages. The time offsets of the reflected and transmitted pulses are determined by

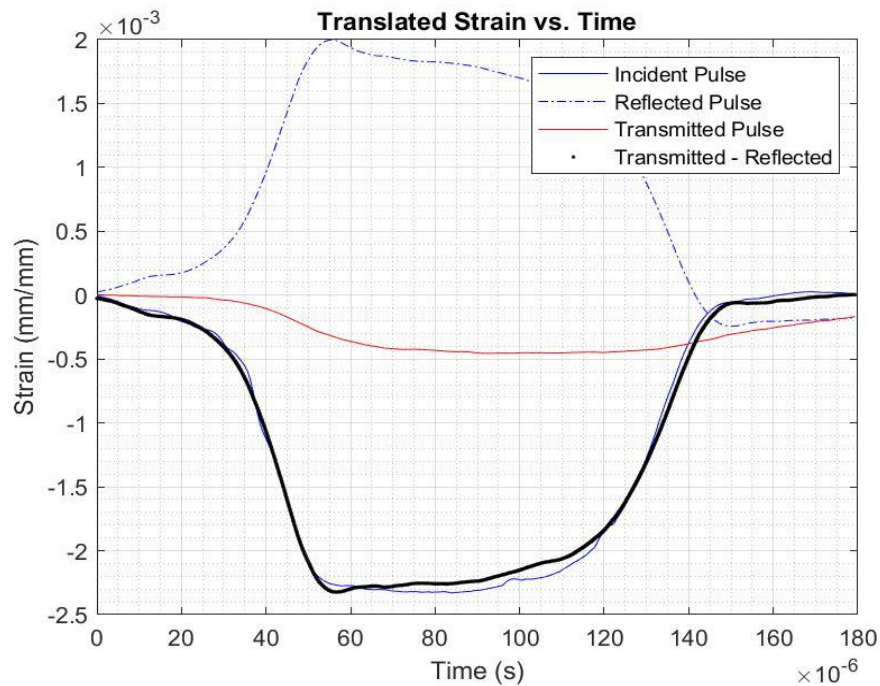


Figure 3.20: Translated incident, reflected, and transmitted waves for a polycarbonate specimen.

$$\tau_R = 2cL_{II} \quad (33)$$

$$\tau_T = cL_{II} + cL_{TI} + c_sL_s \quad (34)$$

where, L_{II} , is the distance from the incident gage to the nearest specimen interface, and, L_{TI} , is the distance from the transmission gage to the nearest specimen interface. If the specimen wave propagation velocity is unknown, an estimate should be used. The three waves, incident, reflected, and transmitted, are plotted after being translated with their respective time delays seen in Figure 3.20. After initial translation, a second algorithm optimizes the position of the reflected and transmitted pulses to best fit the equation $\varepsilon_I = \varepsilon_T - \varepsilon_R$. After the waves have been translated, the one or three wave method may be used to determine stress and strain in the specimen, as appropriate.

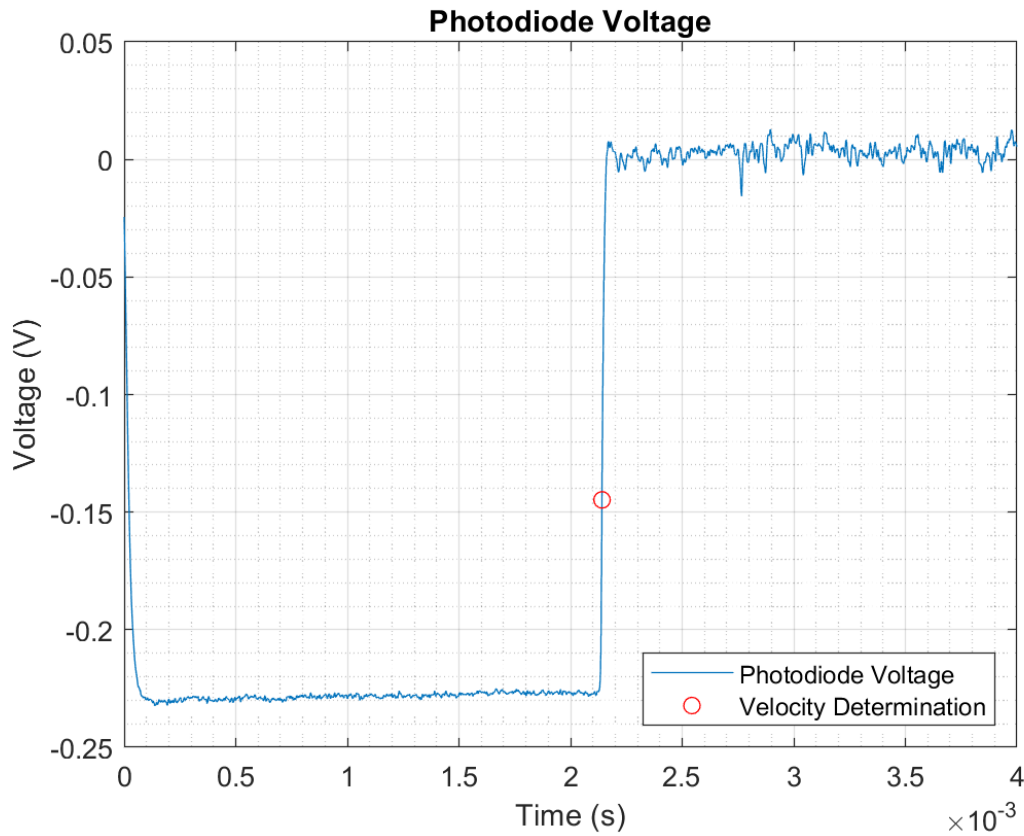


Figure 3.21: Striker velocity determination. Striker crosses laser curtain in 2.141 ± 0.02 ms, resulting in a velocity of 35.6 m/s for a 3" striker bar.

The velocity of the striker is determined by the photodiode. When the laser leading to the photodiode is broken by the striker, the photodiode voltage drops, which triggers the data acquisition. This determines the beginning of the velocity measurement. When the laser is reintroduced, the voltage of the photodiode increases marking the end of the velocity measurement. A Savitzky-Golay filter is applied to the data to smooth the signal. A time derivative of the photodiode voltage is taken. The maximum point in the time derivative is said to be the end of the velocity measurement. An example of velocity measurement data is seen in Figure 3.21.

Chapter 4 – RESULTS AND DISCUSSION

4.1 – System Calibration

Before testing any materials, the SHPB must be thoroughly calibrated to ensure accurate data is produced. The bar wave speed can be estimated knowing the density and elastic modulus of the bar material; however, it is much more accurate to determine the speed experimentally. The bar wave speed is measured by impacting the end of the incident bar when the incident bar is free on both ends. When the incident wave reaches the free end of the bar, the strain wave will be completely reflected. The strain gage will measure both the incident and reflected pulses over time as in Figure 4.1. From this data, the transit time for the pressure wave to propagate twice the distance between the free end of the bar

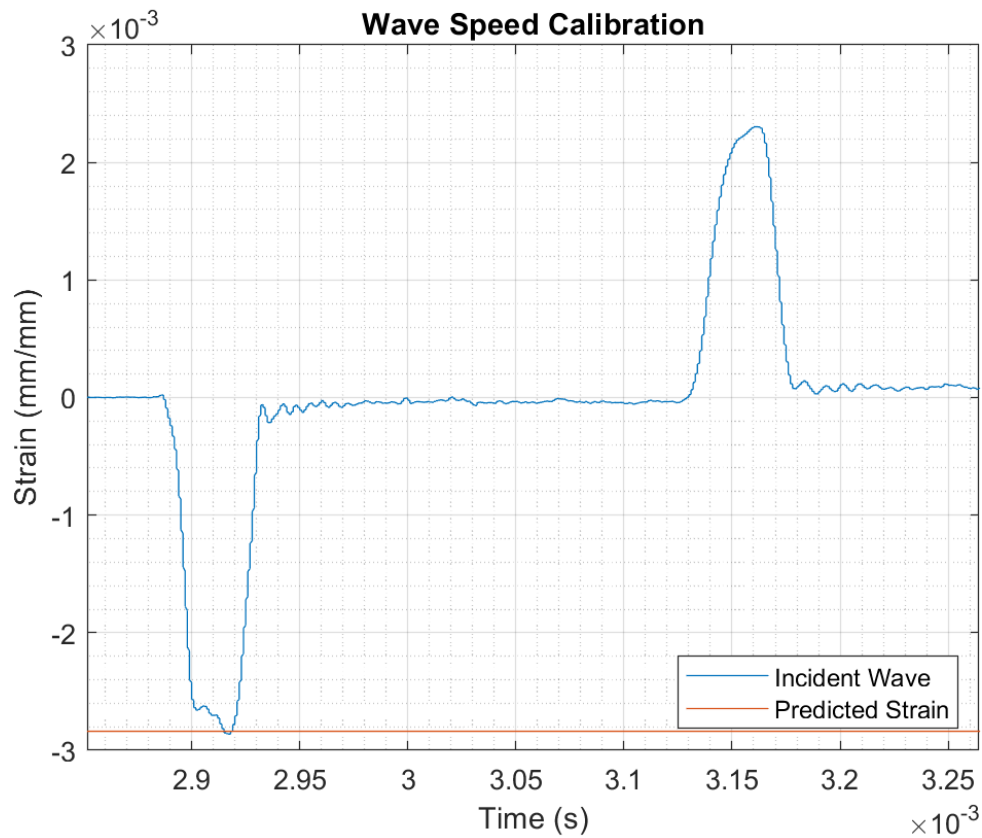


Figure 4.1: Bar wave speed calibration for C350 pressure bars. Time between the start of the incident pulse and start of the reflected pulse is used to calculate wave speed.

and the center of the incident strain gage can be determined. Three runs of the experiment are performed. The results of the experiment can be seen in Table 2. The average wave speed of the C350 pressure bars is determined to be 5160 m/s. The estimated wave speed of aged C350 steel given published nominal values of density and elastic modulus from MatWeb is about 5000 m/s. The experimentally determined speed is used in the SHPB analysis. A similar approach is used to measure the wave speed of the C300 and 7075-T651 bar sets.

Table 2: Experimentally determined wave speed of C350 pressure bars. The uncertainties represent the inaccuracy in the data acquisition equipment.

Trial #	Transit Time – τ (μs)	Calculated Wave Speed - c (m/s)
1	240 ± 0.5	5200 ± 2.4
2	243 ± 0.5	5135 ± 2.5
3	242 ± 0.5	5156 ± 2.5
AVG.	241.7 ± 0.5	5163.3 ± 2.5

The striker velocity measurement is checked against the numerical model. It is important that the striker velocity is accurate as it is used later to calibrate the incident pulse. Several measurements are taken at various initial pressures from 20 psi to 150 psi. The initial pressure is measured with a digital pressure gage with a resolution of 0.1 psi. In Figure 4.2, the striker velocity measurement is compared to the analytical solution and numerical model at different initial pressures. The plot shows results for two striker sizes: 6 inches and 8 inches. Both strikers are made from C300. The measured velocities of the 6-inch striker fall within 2% of the numerical model and within 3% of the analytical solution. The measured velocities of the 8-inch striker fall within 6.5% of the numerical solution and 8% of the analytical solution. As discussed earlier, the velocity measurement

should be taken as close to the end of the barrel as possible, when the striker is closest to its final velocity. When measuring the velocity of a longer striker, the photodiode and laser need to be moved further from the end of the barrel to accommodate the longer length. At this distance, the striker has yet to reach its final velocity, resulting in a lower average velocity during the measurement time. This length dependent error could be eliminated by introducing a second photodiode and laser. In a two laser-photodiode setup, the laser beams will always be a set distance apart, which is independent of the striker length.

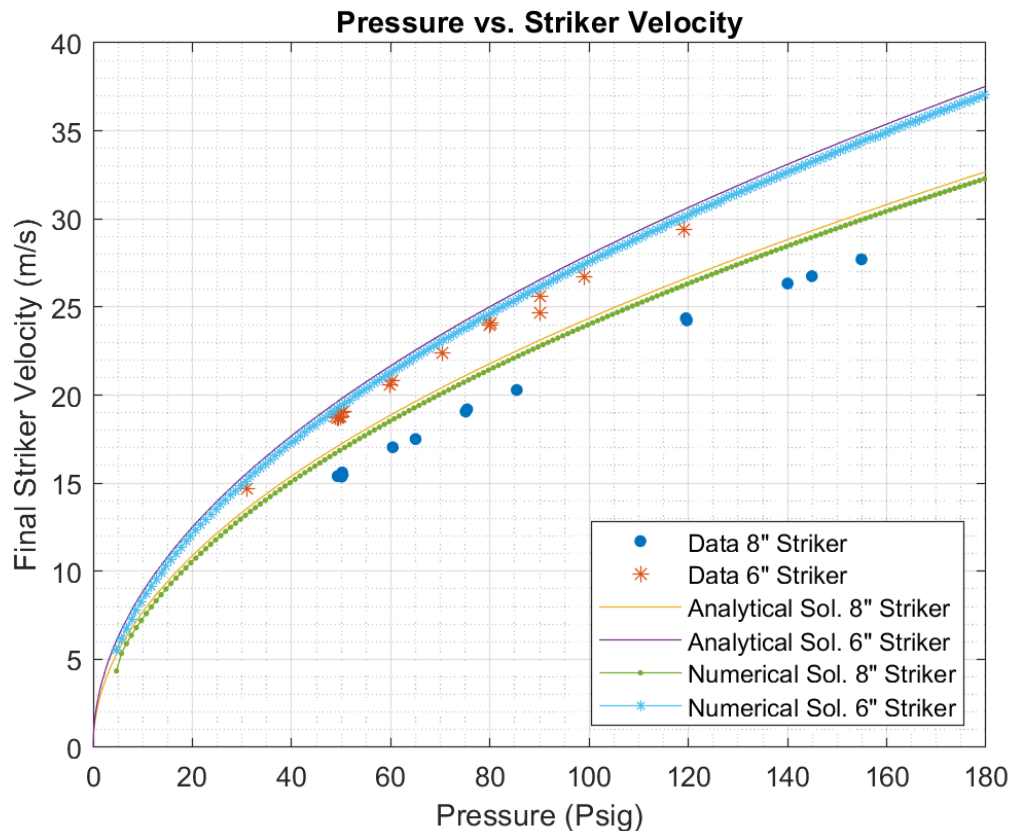


Figure 4.2: Measured and predicted striker velocities vs. initial pressure. The analytical solution and numerical model are shown. Results for two striker lengths are shown.

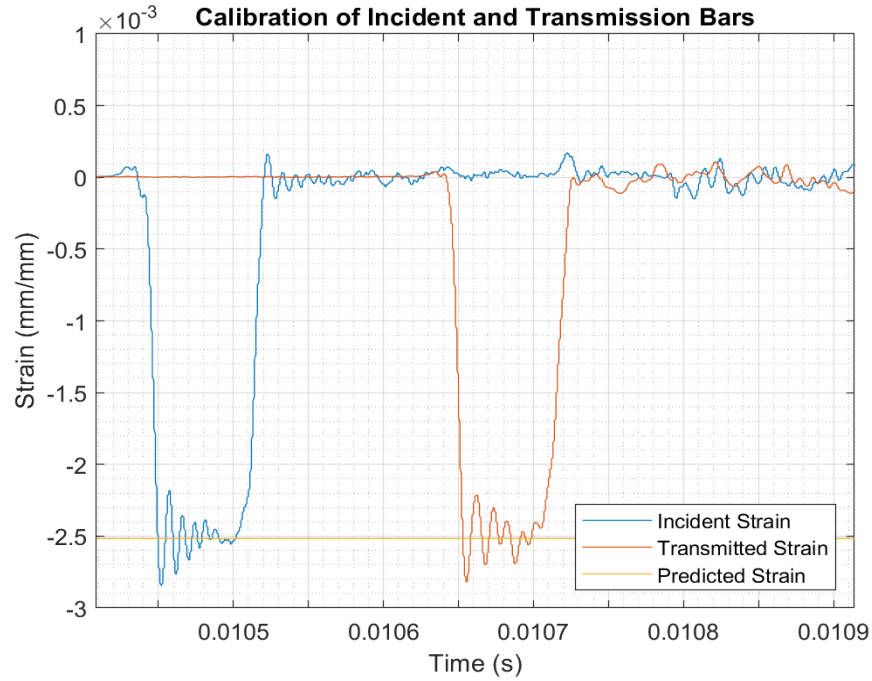


Figure 4.3: Example of calibration test with no specimen. Velocity of striker is 22.6 m/s. The amplitude of the incident and transmitted pulses match the amplitude of the theoretical input strain indicating system is in good calibration.

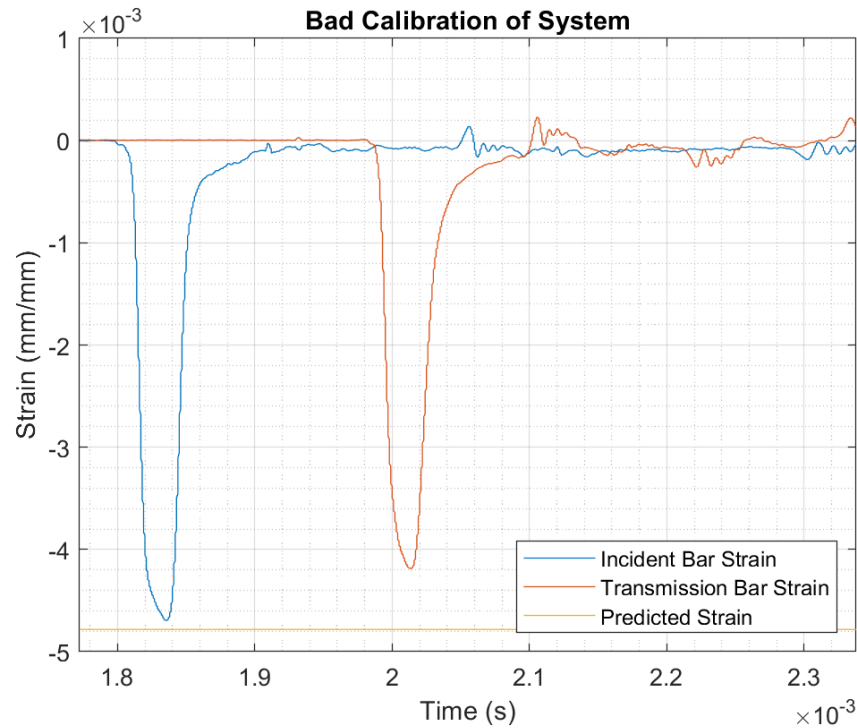


Figure 4.4: Example of bad system calibration. The incident and transmitted pulses fall short of the predicted strain value.

When the striker impacts the end of the incident bar, the amplitude of the incident

strain wave is predicted by (3). The calibration is checked by wringing the incident and transmission bars together with no specimen. If the system is in calibration, the incident and transmitted pulses will approach the calibration value, and there will be no reflected pulse. Figure 4.3 shows a calibration test with no specimen. A striker velocity of 22.6 m/s is measured which predicts a peak strain of 2500 microstrain. Both the incident and transmitted pulses approach the predicted strain indicating good calibration. An example of bad system calibration is seen in Figure 4.4. If the incident, reflected, and transmitted pulses are superimposed onto each other as in Figure 4.5, it becomes clear that the bars are

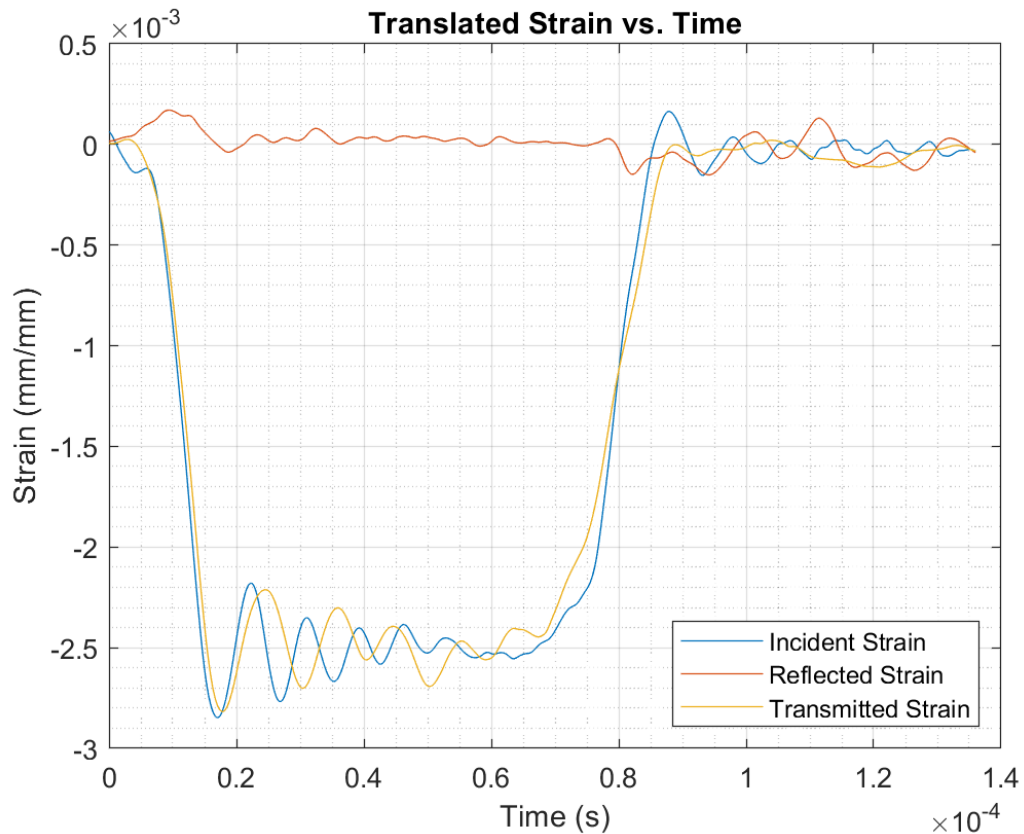


Figure 4.5: Translated incident, reflected, and transmitted waves during a calibration test. The transmitted and incident waves match in amplitude indicating good calibration. The reflected pulse is very close to zero which indicates the pressure bars are in good alignment.

in good alignment; the incident and transmitted pulses match and there is relatively no reflected pulse.

4.2 – Pulse Shaping Effects on Incident Pulse and Dispersion

Pulse shaping is a common technique used to address some of the underlying issues in a SHPB experiment; some of the issues being dispersion, non-constant strain rate, and stress imbalance [21]. The pulse shaper is essentially a dummy specimen placed between the incident bar and striker bar. The plastic deformation of the dummy specimen filters out high frequency components of the incident pulse resulting in a more gradual trapezoidal incident pulse. In general, the pulse shaper is made from soft materials such as copper or soft aluminum [1]. By varying the thickness and diameter of the pulse shaping discs, different waveforms can be achieved. The pulse shapers used in these experiments are made from 1100 series aluminum. The pulse shapers are made by stamping discs from sheets of aluminum, 0.8 mm in thickness. Two sizes of pulse shaper are 3.18 mm and 6.35 mm. To investigate the effects of the pulse shapers, the incident and transmission bars are wrung together, similar to a calibration test. The pulse shaper is placed on the front of the incident bar and is held in place by petroleum jelly, which acts as an interfacial lubricant. Figure 4.9 shows a pulse shaper mounted on the bar. Figure 4.6 shows the effect of the

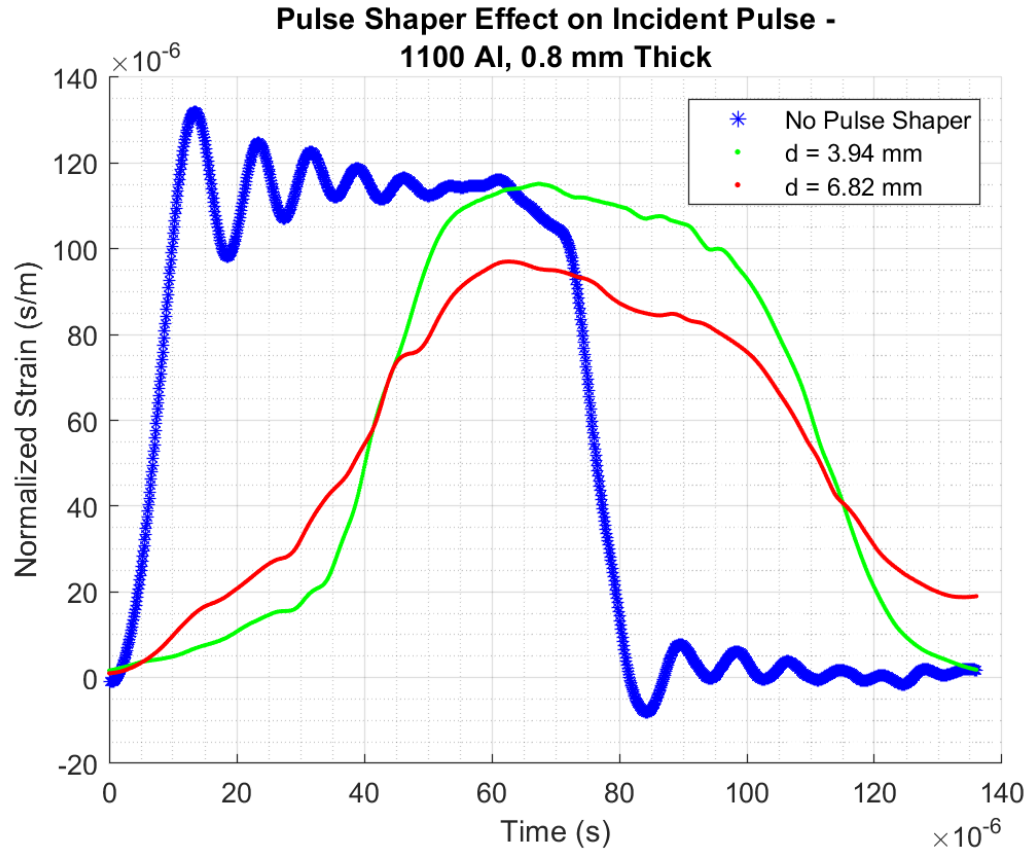


Figure 4.6: Pulse shaper effect on incident pulse. The strain is normalized by the striker velocity.

pulse shaper on the incident wave. The pulse shapers extended the loading duration of the incident pulse from 80 μ s to 135 and 205 μ s for 3.94 mm and 6.82 mm pulse shapers, respectively. This is useful to extend the loading duration of the specimen, when a longer striker cannot be used. The pulse shapers also reduce the amplitude of the incident pulse since they absorb some of the impact of the striker bar.

One of the more useful effects of the pulse shaper is reducing dispersion by filtering out the high frequency components of the incident wave. In theory, the incident and transmitted waves of the test should be the same; however, the waveform changes as it propagates along the rods due to dispersion. Figure 4.7 shows the difference between the incident and transmitted waves for a non-pulse shaped and pulse shaped test. The pulse shaper reduced the variance in the difference of the two waves by more than an order of magnitude from 10^{-11} to 10^{-12} . Using a fast Fourier transform, the frequency spectrum of a non-pulsed shaped incident wave and pulse shaped incident wave can be compared, as in

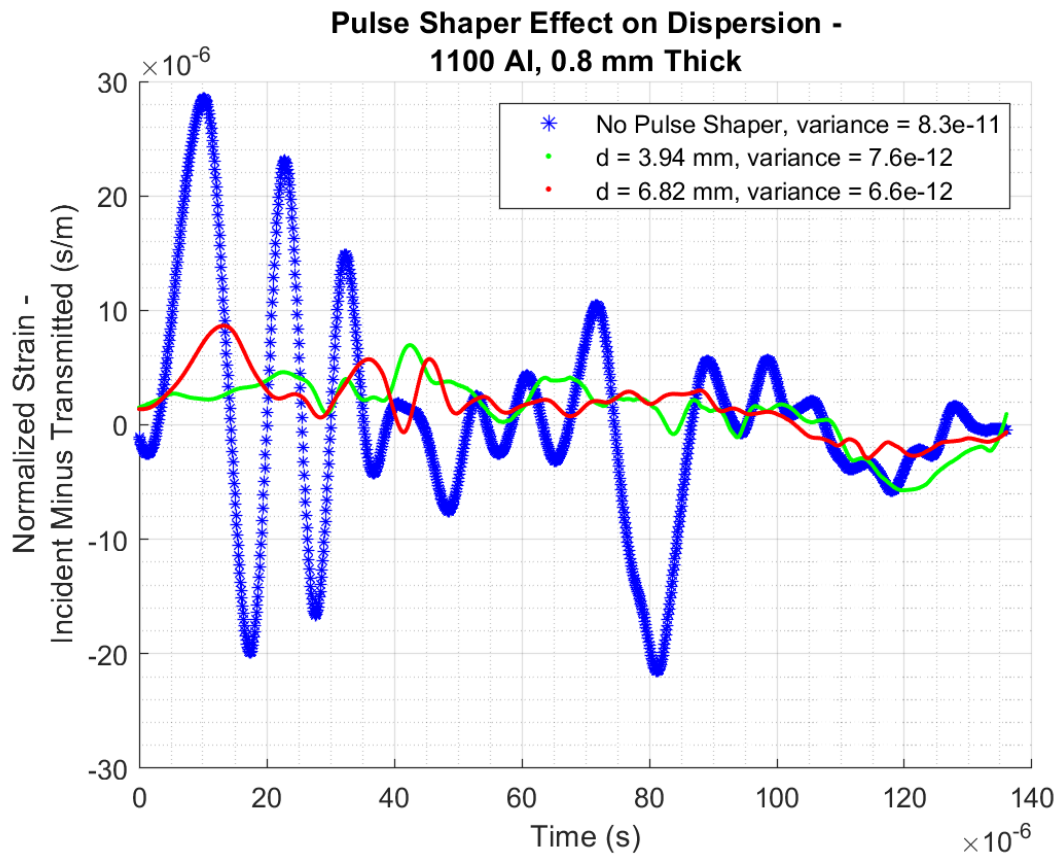


Figure 4.7: Pulse shapers reducing the variance between the incident and transmitted pulses.

Figure 4.8. The frequency spectrum shows how the pulse shaper acts as a low pass filter, filtering out the high frequency components that are susceptible to dispersion.

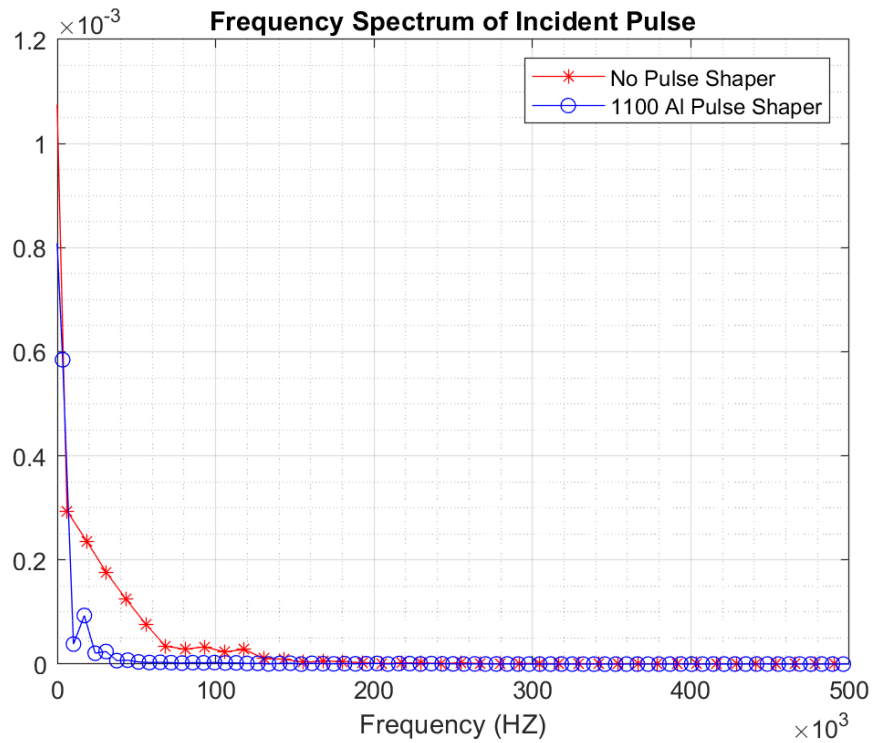


Figure 4.8: Frequency spectrum of a non-pulsed shaped incident pulse and a pulse shaped incident pulse. The pulse shaper acts as a low pass filter.

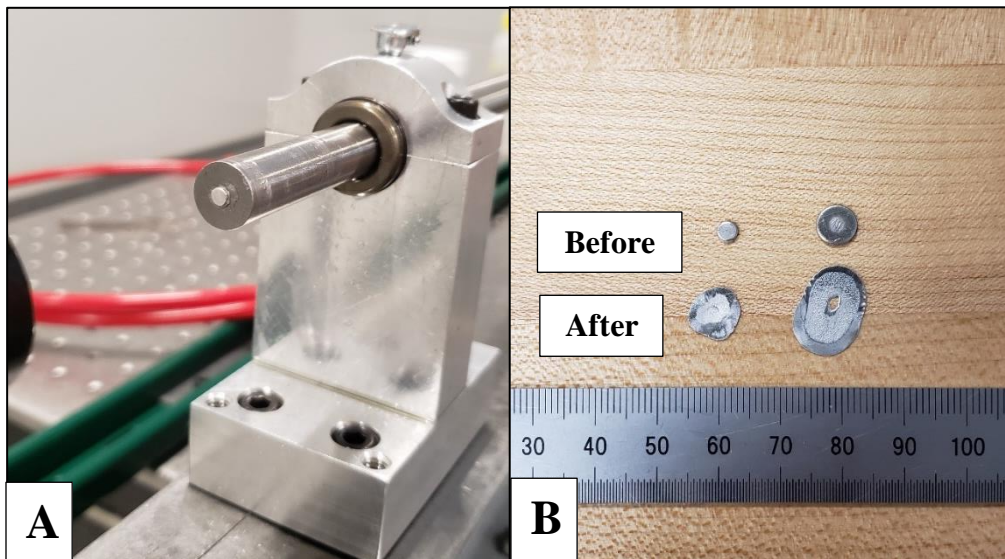


Figure 4.9: **A.** Pulse shaper loaded on the incident bar. **B.** Pulse shapers before and after use.

4.3 – Dynamic Response of Al 6061-T6511

Aluminum 6061-T6511 alloy specimens are tested at strain rates between 1000 s^{-1} and 6300 s^{-1} with the axis of compression in line with the extrusion axis of the specimens. Specimens are prepared from cylindrical bar stock with nominal diameter of 7.94 mm. The specimens are cut to various lengths between 2.5 mm and 5.2 mm. The faces are lapped flat and parallel to prevent tilt effect. The initial length and diameter of each specimen is recorded. The SHPB facility is setup with C300 pressure bars and an 8-inch striker bar. A calibration test is performed prior to testing to verify the alignment of the bars.

Each specimen is loaded into the SHPB between the incident and transmission bars and lubricated with petroleum jelly. Careful placement of the specimen ensures that the center axis is aligned with pressure bars center axis. An 1100 Aluminum pulse shaper is used for all tests. The strain rate of each test is varied by changing the initial length of the specimen and the striker velocity. The tests are summarized in Table 3.

Table 3: Table of 6061-T6511 test specimens.

SN	Initial Length (mm)	Initial Diameter (mm)	Striker Velocity (m/s)	Experimental Strain Rate (s^{-1})
1	5.15	7.85	15.51	1029
2	5.16	7.86	15.45	1048
3	5.21	7.86	17.53	1398
4	3.95	7.85	19.10	2133
5	3.98	7.85	20.31	2370
6	3.86	7.85	24.25	3534
7	3.32	7.85	24.35	3927
8	3.24	7.85	26.79	4700
9	2.56	7.85	26.74	5836
10	2.51	7.85	27.67	6308

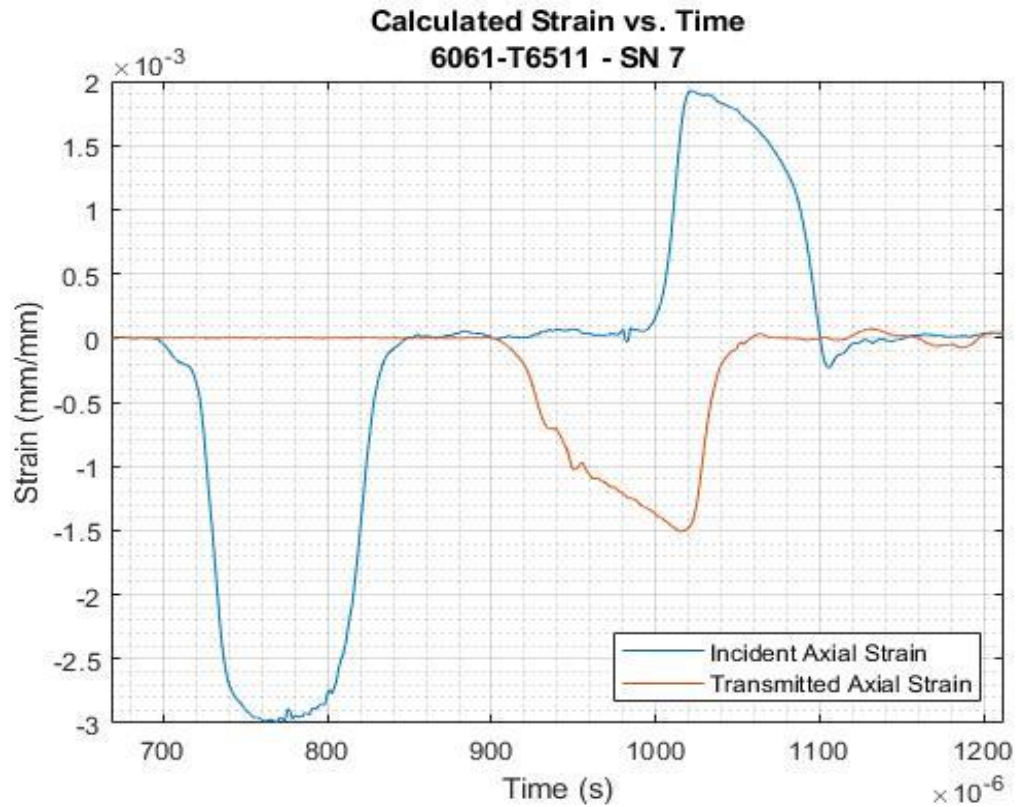


Figure 4.10: Incident and transmitted bar strains from test sample SN 7.

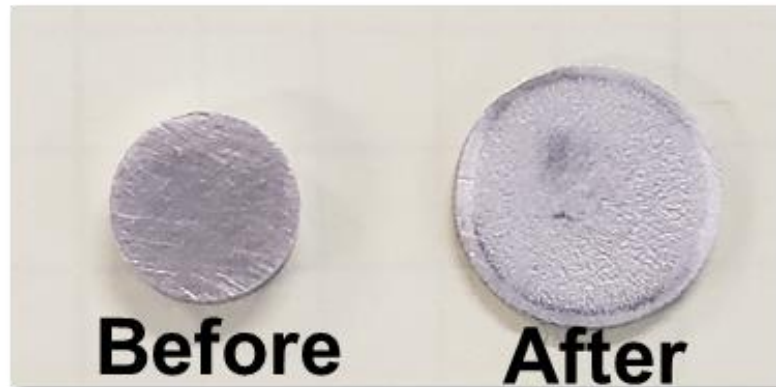


Figure 4.11: Aluminum specimens before and after dynamic compression.

The pressure bar data for SN 7 is shown in Figure 4.10. The blue curve shows the strain recorded by the incident bar strain gage and the red curve shows the strain recorded by the transmission bar strain gage. The first blue trapezoidal wave is the incident pulse.

Notice that the amplitude is negative indicating compression. After some time, the same gage measures the reflected wave which is seen as the second blue trapezoidal wave. Notice that the amplitude is now positive indicating tension. The red curve shows the transmission bar strain, which under the assumption of uniform stress is proportional to the stress in the specimen over time. Figure 4.11 shows an aluminum specimen before and after testing. The specimen is flattened and expands due to Poisson's effect.

After translating the waves to represent the strains at the bar interfaces, the specimen strain can be obtained as in Figure 4.12. The three and one wave methods of calculating strain are shown. The one wave method produces a nearly identical curve to the

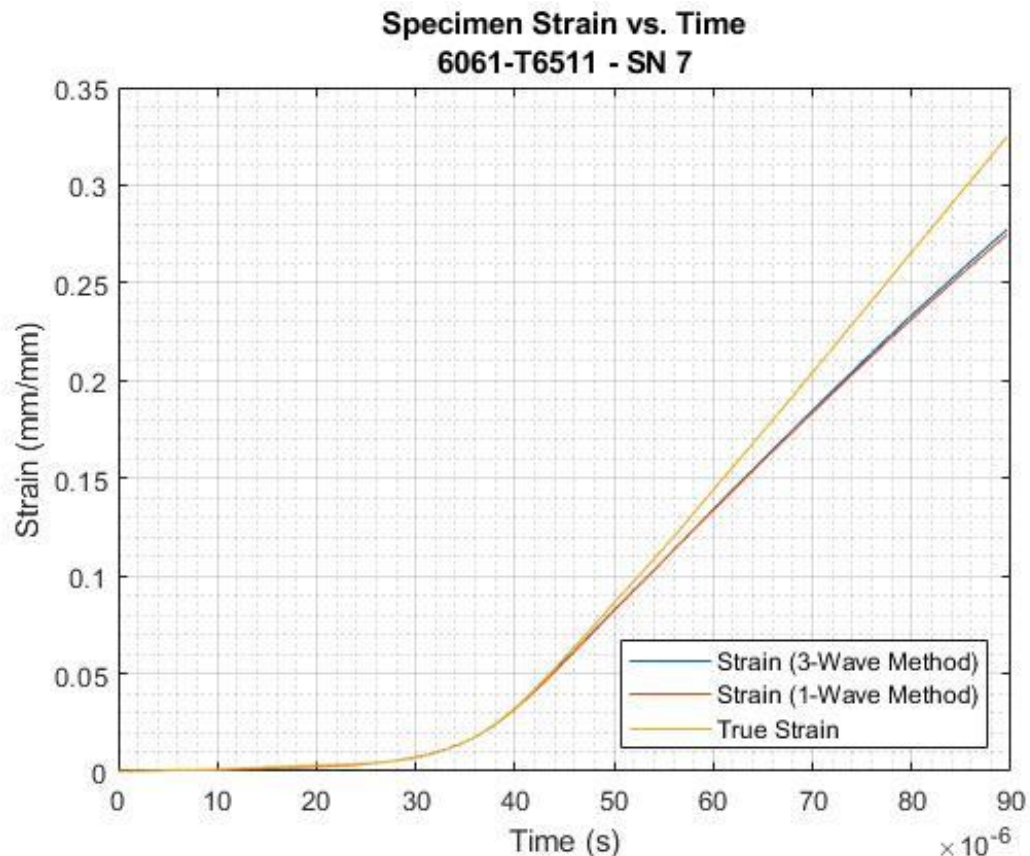


Figure 4.12: Strain in specimen SN 7 over time. Both three and one wave methods are shown. The true strain corrects for the Poisson's effect.

three-wave method which indicates that the specimen was in stress equilibrium throughout the loading.

The strain rate of the experiment can be deduced from the reflected wave if the specimen is in stress equilibrium. Figure 4.13 shows the strain rate versus time for specimen SN 7. During initial loading, the specimen deforms at a nonconstant strain rate loading, but after 40 μs , deforms at a relatively constant strain rate. The three and one wave methods agree; however, the one-wave method is more stable. An average of the true strain rate over the loading duration is used to report test results. The average strain rate for 6061-T6511 specimen SN 7 is 3587 s^{-1} .

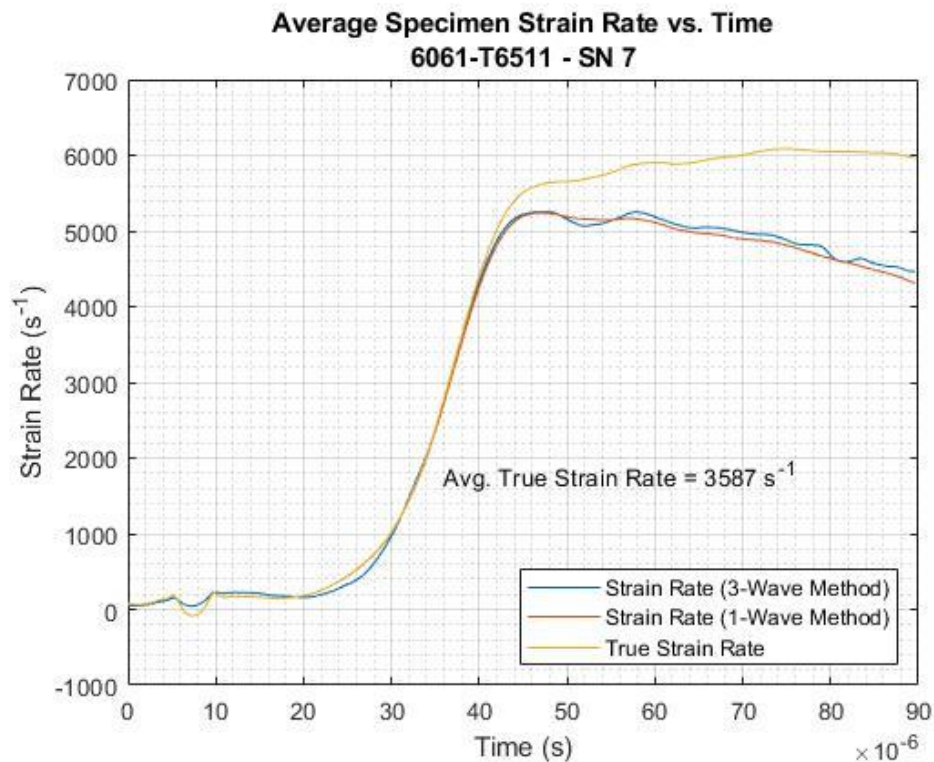


Figure 4.13: Strain rate of test specimen 6061-T6511 SN 7. Constant strain rate is achieved after 40 μs .

The dynamic stress-strain curves for the ten specimens are shown in Figure 4.14. The specimens yield at about 300 MPa which is much higher than the quasi-static yield strength of 253 MPa. For many materials, it is expected that the yield strength is greater under dynamic loading conditions. After yielding, the material exhibits strain hardening behavior up to about 10% strain. The flow stress after the strain hardening region remains relatively constant. In general, the flow stress increases as strain rate increases. The flow stress is about 350 MPa at 1000 s^{-1} , and 400 MPa at 6000 s^{-1} . Strain rate dependency is usually reported at a constant strain as in [45]. Figure 4.15 shows the flow stress strain rate dependency of 6061-T6511 at 25% strain. The flow stress increases with strain rate linearly at a rate of about 0.009 MPa-s.

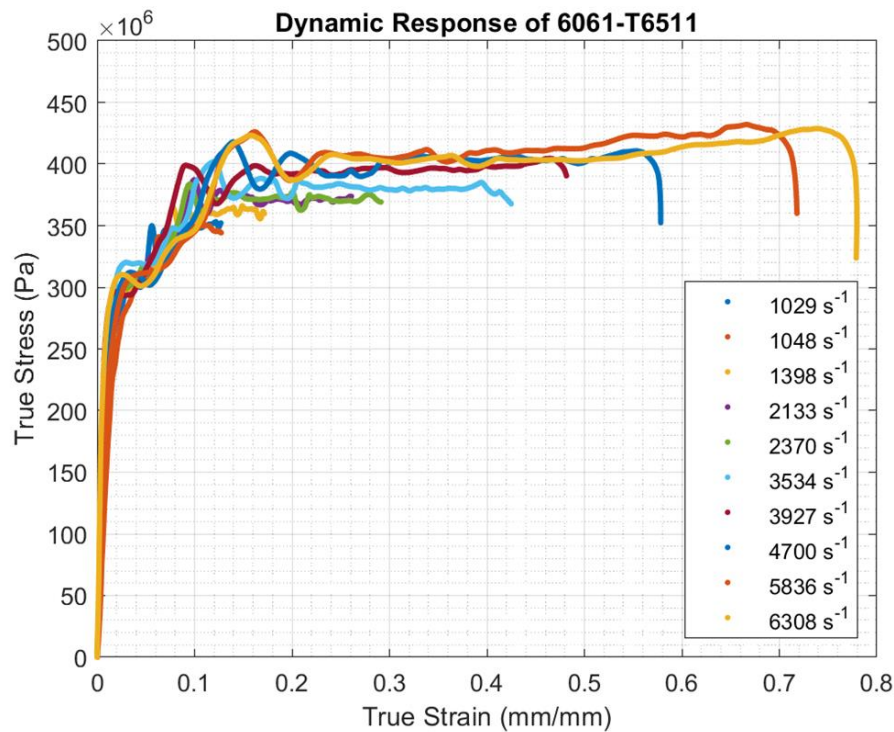


Figure 4.14: Dynamic response of 6061-T6511 Aluminum Alloy over a range of strain rates.

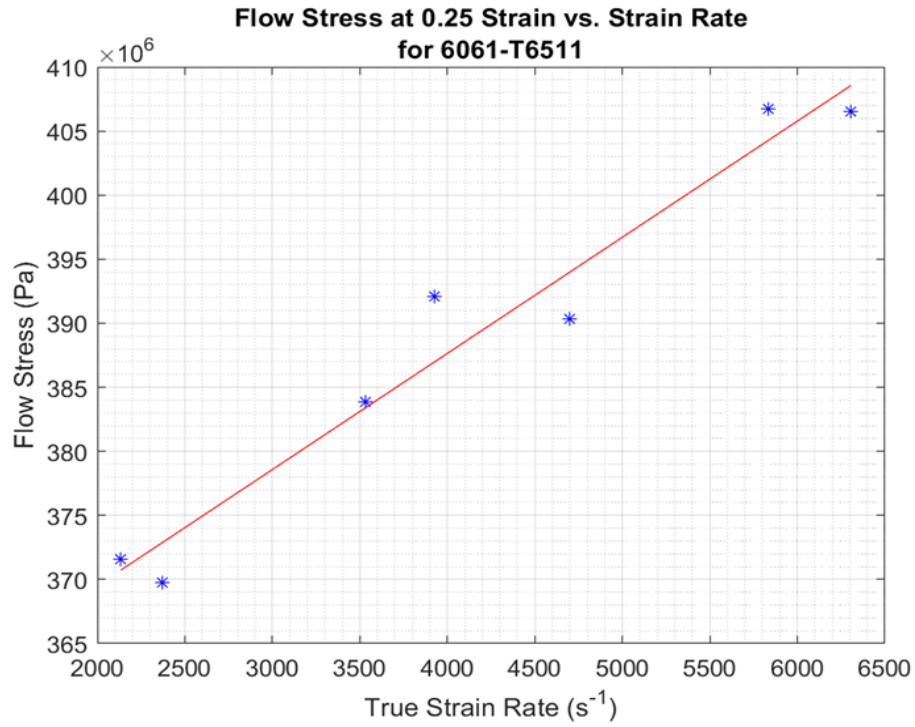


Figure 4.15: Flow stress strain rate dependency of 6061-T6511 at 25% strain.

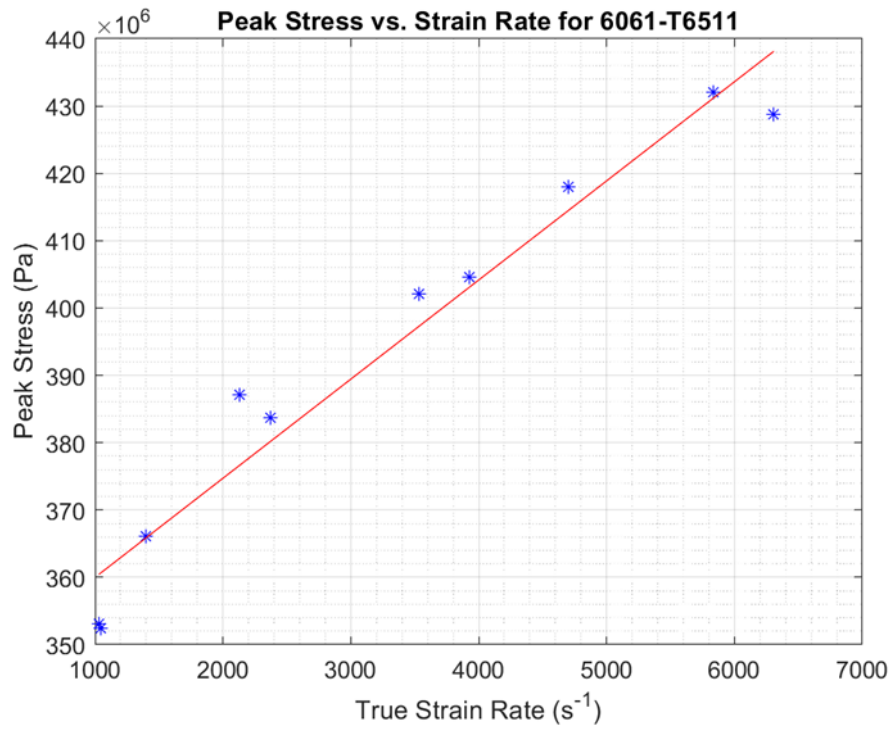


Figure 4.16: Peak stress strain rate dependency for 6061-T6511 between $1000 s^{-1}$ and $3000 s^{-1}$.

The peak stress for each stress-strain curve exhibits similar behavior. In general, the peak stress increases as the strain rate increases as in Figure 4.16. The rate of increase is about 0.015 MPa-s. This behavior is consistent with literature [46-49].

4.4 – Dynamic Response of Polycarbonate

Polycarbonate (PC) is a material well known for its impact strength. PC has been well studied, making it an ideal candidate to validate the current SHPB. Eight PC specimens are prepared with lengths ranging from 2.5 mm to 6.5 mm. The initial diameter of each specimen is 9.52 mm. The specimens are summarized in Table 4. The PC specimens are tested between strain rates of 1300 s^{-1} and 7000 s^{-1} . The faces are lapped flat and parallel to prevent tilt effect. The initial length and diameter of each specimen is recorded. The SHPB facility is setup with C300 pressure bars. An 8-inch striker bar is used for specimen SN 1 to 3, and a 6-inch striker is used for specimen SN 4 to 8. A calibration test is performed prior to testing to verify the alignment of the bars. The polycarbonate specimen is seen before and after a SHPB experiment in Figure 4.17.

Table 4: Table of Polycarbonate specimens.

SN	Initial Length (mm)	Initial Diameter (mm)	Striker Velocity (m/s)	Experimental Strain Rate (s^{-1})
1	6.33	9.51	15.35	1367
2	6.12	9.52	17.07	1666
3	6.51	9.52	19.19	1902
4	3.92	9.52	20.61	2430
5	3.87	9.52	22.40	2538
6	3.60	9.52	24.09	2960
7	3.79	9.52	25.60	4388
8	2.51	9.52	24.64	7077

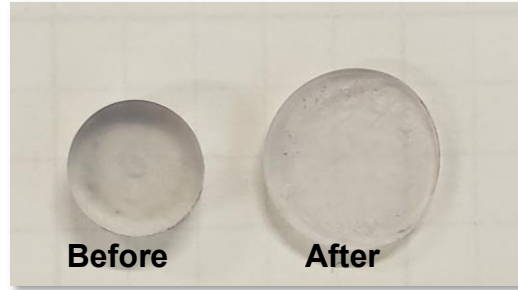


Figure 4.17: Polycarbonate specimen before and after SHPB experiment.

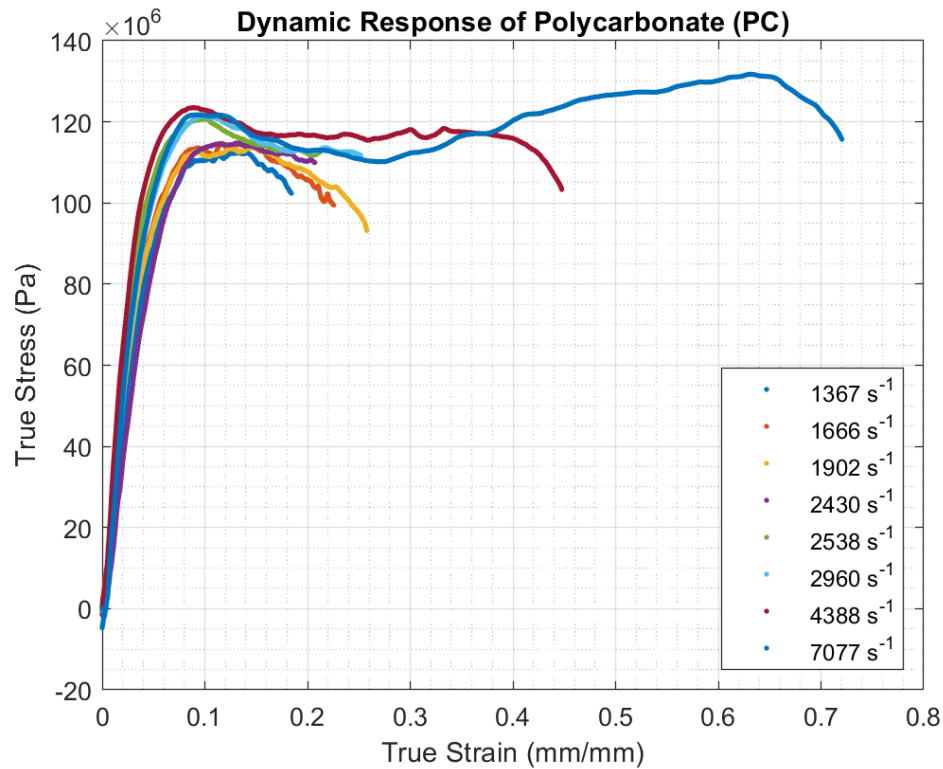


Figure 4.18: Dynamic stress-strain curves of Polycarbonate.

The dynamic stress-strain curves of the PC specimens are shown in Figure 4.18. The yield strength of polycarbonate is strain rate dependent, tending to increase as strain rate increases. The yield strength is between 110 MPa and 124 MPa for strain rates between 1300 s^{-1} and 7000 s^{-1} . After initial yield, the polycarbonate exhibited softening behavior up to about 30% strain, then began hardening. This is most evident at the higher strain rate tests. The stress-strain curves match those found in literature [2], as in Figure 4.19.

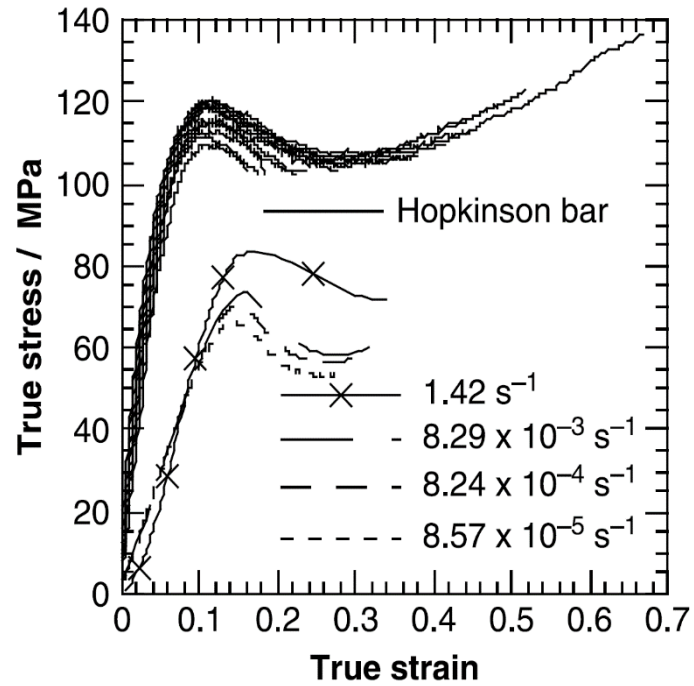


Figure 4.19: Stress-strain curves of polycarbonate. Reproduced from Siviour, C. R. et al. [2].

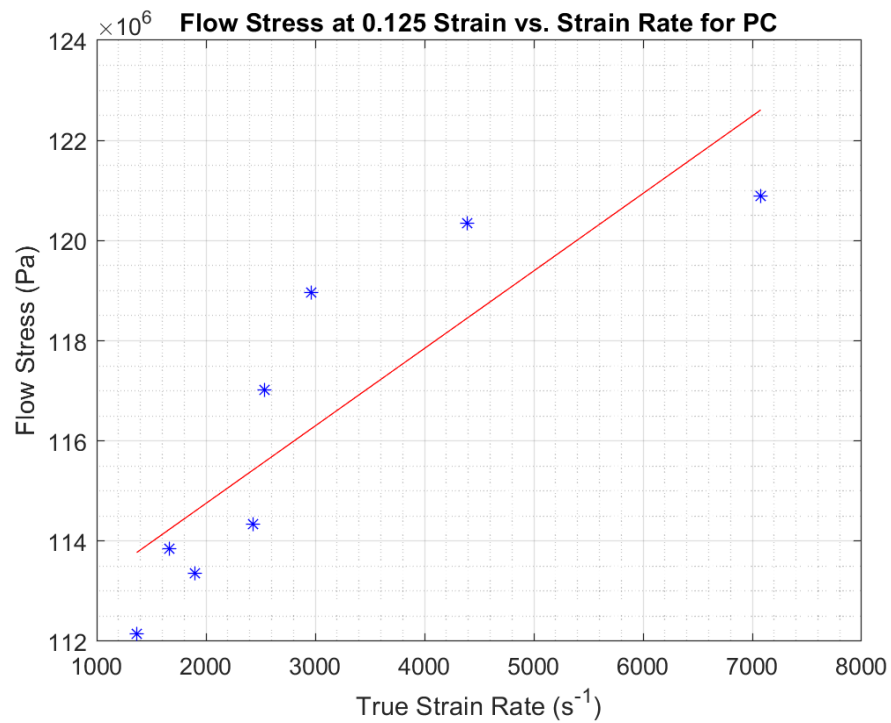


Figure 4.20: Flow stress of PC specimens at 12.5% strain at various strain rates.

Polycarbonate shows some strain rate dependent behavior in flow stress as in Figure 4.20. As strain rate increases, the flow stress at 12.5% strain increases at a rate of about 0.0016 MPa-s. Similarly, the peak stress is strain rate dependent, increasing at a rate of about 0.0033 MPa-s, as in Figure 4.21.

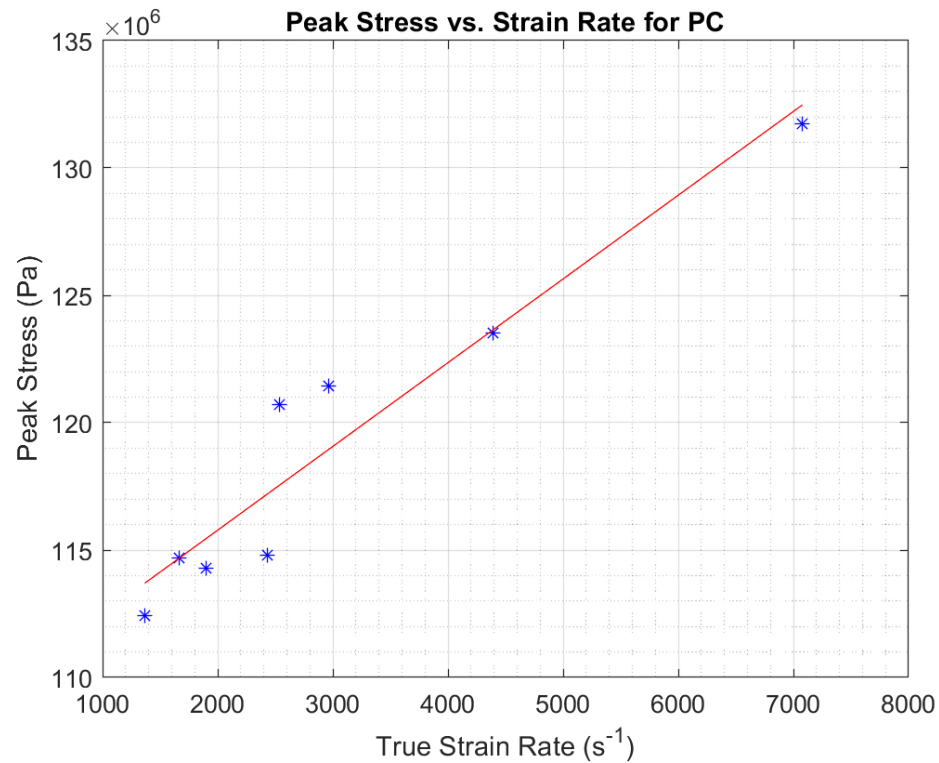


Figure 4.21: Peak stress of PC specimens at various strain rates.

4.5 – Dynamic Response of SAC and SAC + CNT

Super Activated Carbon (SAC) is an inherently soft material, requiring special care when designing a SHPB experiment. SAC is about 1% carbon by volume, the rest being void. The elastic modulus of SAC is on the order of 10's of megapascals and has an ultimate strength of about 10 MPa. SHPB tests on soft materials result in very weak transmitted waves, requiring soft pressure bars to amplify the signals. For testing SAC, Aluminum 7075-T651 pressure bars are used. The soft pressure bars amplify the signal by about three times compared to C300 pressure bars. Additionally, the gain is increased for the transmission bar strain gage to further distinguish the signal from noise. An example of the incident, reflected, and transmitted waves for SAC is Figure 4.22.

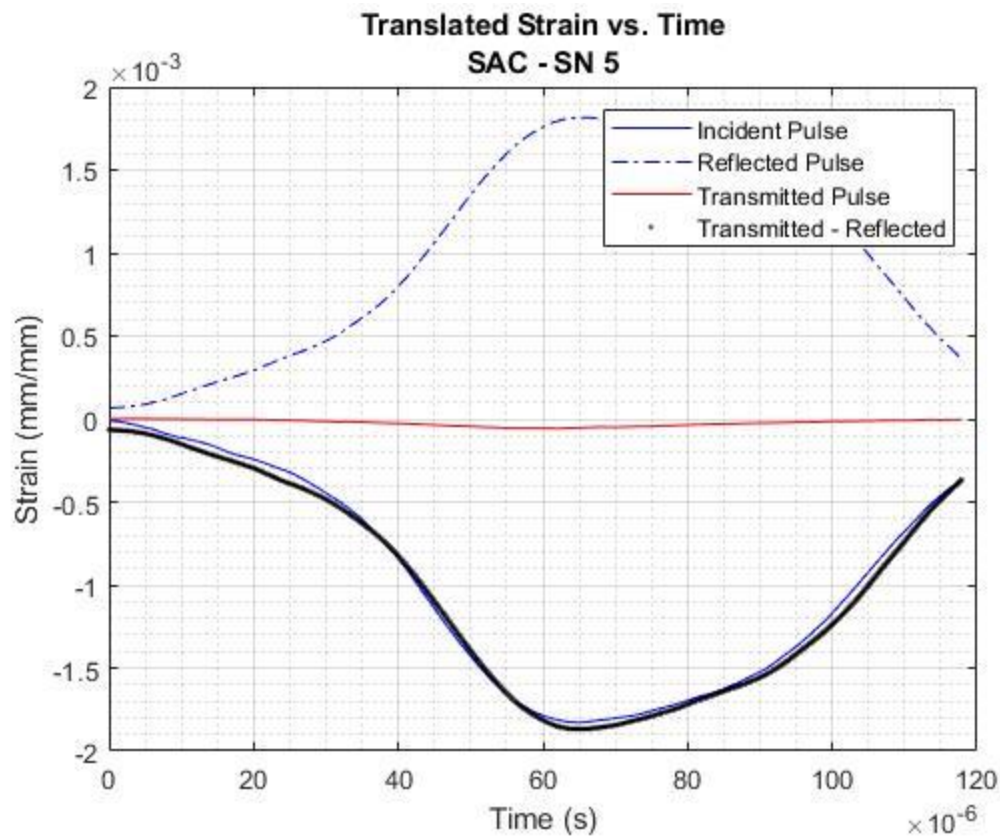


Figure 4.22: Translated strain waves of SAC specimen SN 5. The transmitted signal is very weak compared to the incident and reflected signals, which closely match.

SAC with Carbon Nanotube (SAC + CNT) is a SAC matrix composite reinforced by carbon nanotubes. The CNTs reinforce the pores within the matrix. This composite is 2% carbon by volume. Specimens for both SAC and SAC + CNT are prepared and summarized in Table 5 and Table 6, respectively.

Table 5: Table of Super Activated Carbon (SAC) specimens.

SN	Initial Length (mm)	Initial Diameter (mm)	Striker Velocity (m/s)	Experimental Strain Rate (s^{-1})
1	5.38	7.86	12.25	1151
2	5.35	7.83	13.69	1366
3	5.36	7.86	13.55	1386
4	5.42	7.86	16.58	1760
5	5.40	7.84	16.65	1800
6	4.93	7.81	19.48	2450
7	5.38	7.85	21.53	2524
8	5.39	7.83	24.92	3015
9	4.87	7.83	27.50	3814

Table 6: Table of Super Activated Carbon + CNT (SAC + CNT) specimens.

SN	Initial Length (mm)	Initial Diameter (mm)	Striker Velocity (m/s)	Experimental Strain Rate (s^{-1})
1	5.48	7.86	12.16	1089
2	5.44	7.85	15.09	1533
3	5.50	7.79	19.80	2199
4	5.42	7.85	21.70	2495
5	5.30	7.80	24.55	3030
6	5.45	7.85	26.89	3271

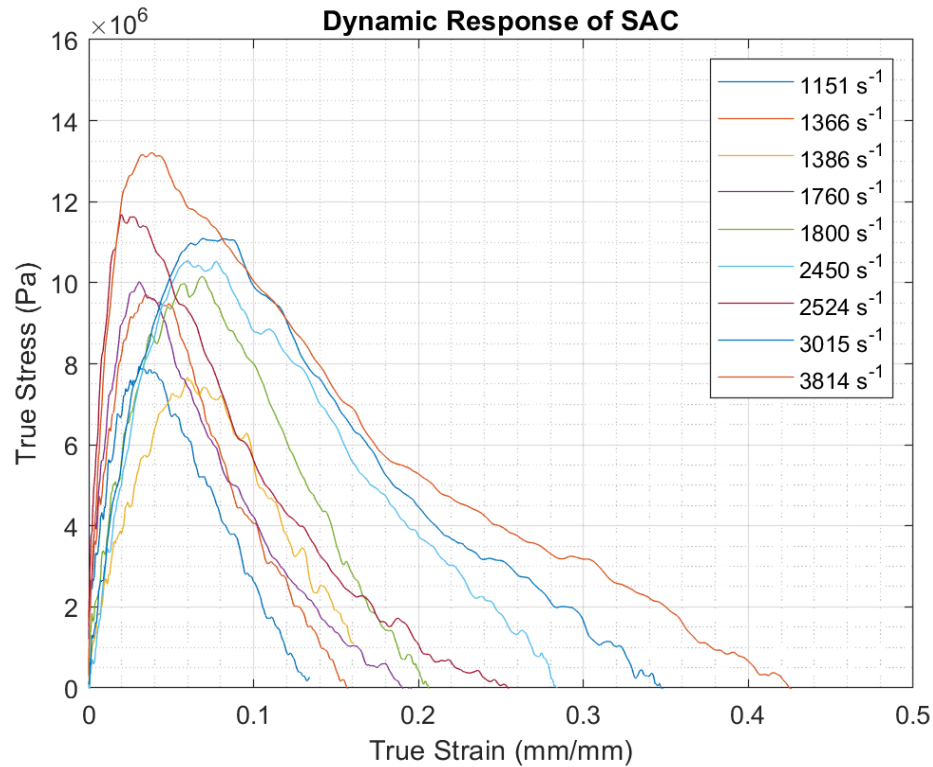


Figure 4.23: Dynamic response of SAC at various strain rates.

Experiments on SAC are conducted at strain rates between 1000 s^{-1} and 4000 s^{-1} . The dynamic stress-strain curves of SAC are shown in Figure 4.23. SAC demonstrates some rate dependency. By looking at the peaks of the stress-strain curves, it is quickly deduced that the peak stress increases as strain rate increase. The dynamic stress-strain curves for SAC + CNT are shown in Figure 4.24. The stress-strain curves for SAC + CNT are inconsistent and make it difficult to find patterns. This is likely attributed to the specimen preparation. The SAC + CNT specimens do not have flat and parallel faces which introduce stress concentrations, violating the uniform stress assumption. The stress measurements remain relatively accurate though since the stress equations are less sensitive to violations of this assumption. By plotting the peak stress versus strain rate for SAC and SAC + CNT in Figure 4.25, it becomes clear the SAC is rate dependent. The peak stress for SAC increases by about 60% over the strain rate range of 1000 s^{-1} to 4000 s^{-1} . SAC +

CNT shows the opposite behavior, decreasing in peak stress by about 9% from 1000 s^{-1} to 3200 s^{-1} . The decrease in peak stress may be attributed to the CNT additive in the SAC. CNTs are inherently hard, making them brittle. As the strain rate increases, the CNTs that line the pores of the SAC break, requiring less stress to deform the material.

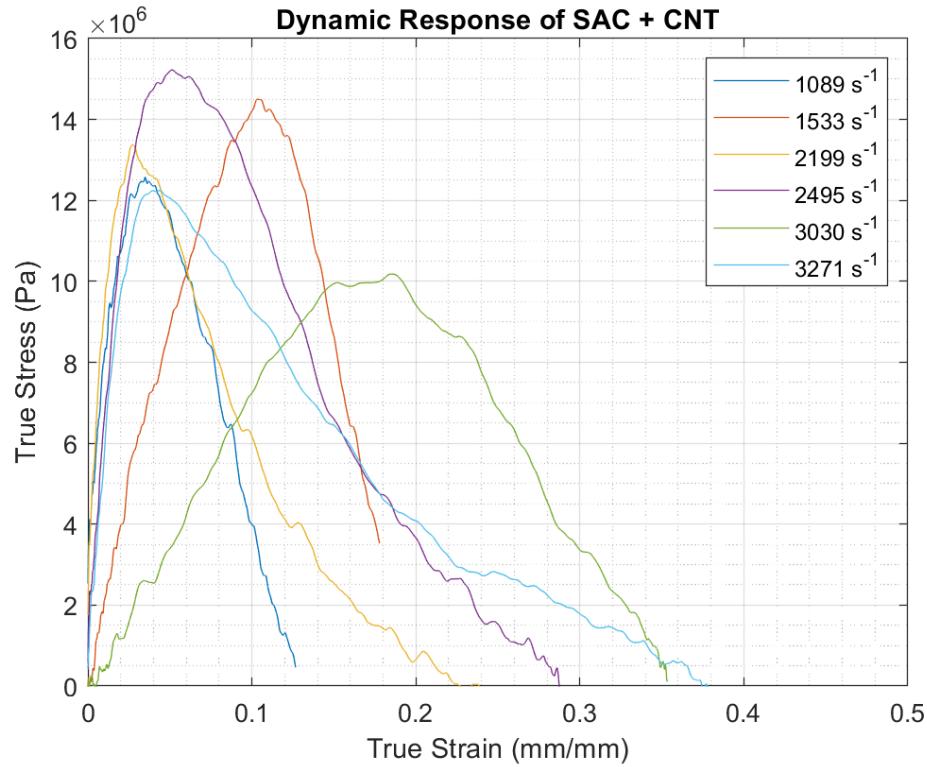


Figure 4.24: Dynamic response of SAC + CNT composite.

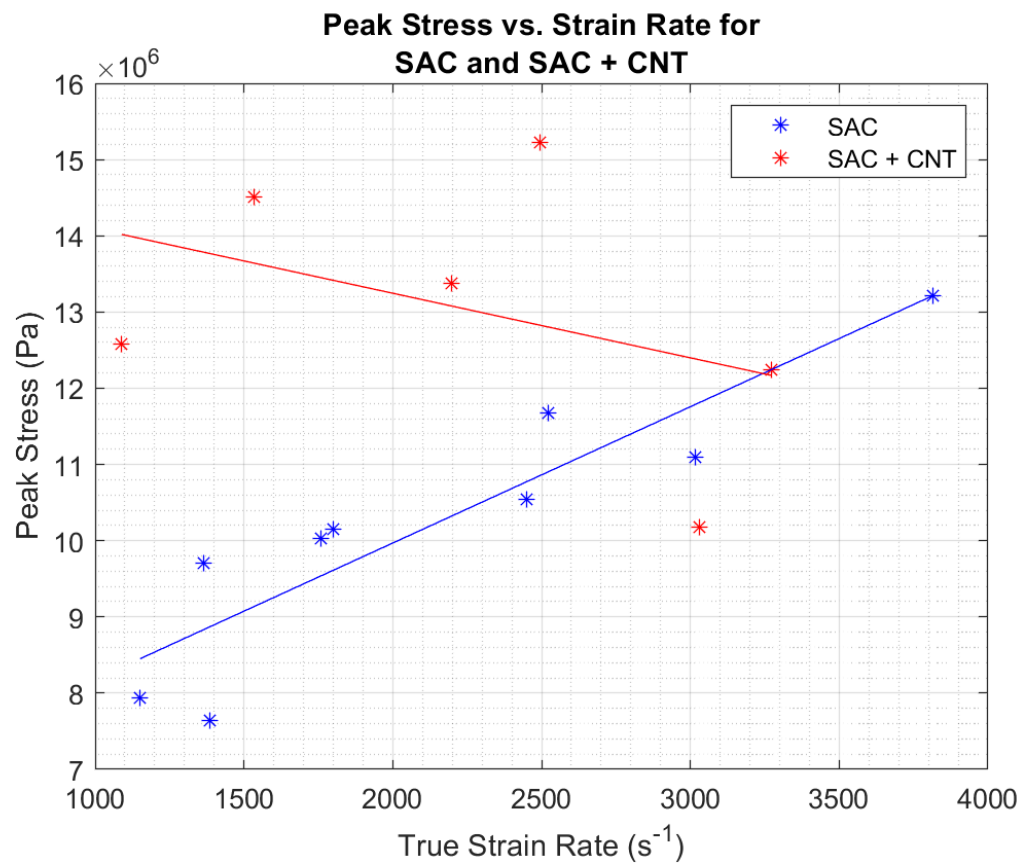


Figure 4.25: Peak stress versus strain rate for SAC and SAC + CNT.

Chapter 5 – CONCLUSIONS

The Split Hopkinson Pressure Bar is a widely accepted experiment for investigating the dynamic response of materials. Over the last 70 years, many improvements have been made to study materials more accurately and to broaden the envelope of materials that can be tested using the SHPB. The presented SHPB facility was designed to encapsulate the many years of research which have gone into improving the experiment.

The current design features three sets of pressure bars which can be used to characterize materials from soft polymers to hard ceramics and even composite materials. The bearings allow the pressure bars to be swapped without a need for realigning the system, which saves significant time when setting up a new experiment. A numerical model was created to understand the design of the gas gun system as well as predict striker velocity more accurately. The robustness of the gas gun system allows many different lengths of strikers to be used with velocities exceeding 150 m/s. It is common for strain gages to break during the experiment which is usually the limiting factor to the maximum attainable strain in the system. The strain gage design presented improved the upper limit of the striker velocity from 40 m/s in previous works to at least 50 m/s. The strain gage used is a tee rosette style allowing for the simultaneous measurement of axial and transverse strain which may allow for more robust analysis of the material specimen. The data acquisition system was designed to be easy to use in order to simplify testing. LabVIEW control software was written to control the operation of the SHPB as well as control data acquisition. A sampling rate of 20 MHz and frequency response of 500 kHz allows the system to capture strain data even for short load durations. Typical load durations are 100 μ s.

The bars are shown to be well aligned through a calibration test with no specimen. The bars maintain alignment even through many tests. Testing of a widely studied material 6061-T6511 showed that the system is capable of reproducing data. Strain rate dependency was shown in the strain rate range of 1000 s^{-1} to 6300 s^{-1} . The yield strength as well as flow stress of the alloy increased with strain rate. The yield stress increased from 253 MPa during quasi-static testing to about 300 MPa during a SHPB experiment. The strain hardening rate was shown to decrease exponentially with increasing strain rate. Polycarbonate, another well studied material, was compared to published SHPB data. The yield strength and flow stress increase with strain rate for PC. The test showed that polycarbonate softens after yield, then hardens after about 30% strain, which is consistent with literature. SAC and SAC + CNT materials were tested using soft pressure bars, showing the use of aluminum pressure bars. SAC was found to increase in strength as strain rate increased. The strength of SAC + CNT decreased slightly as strain rate increased.

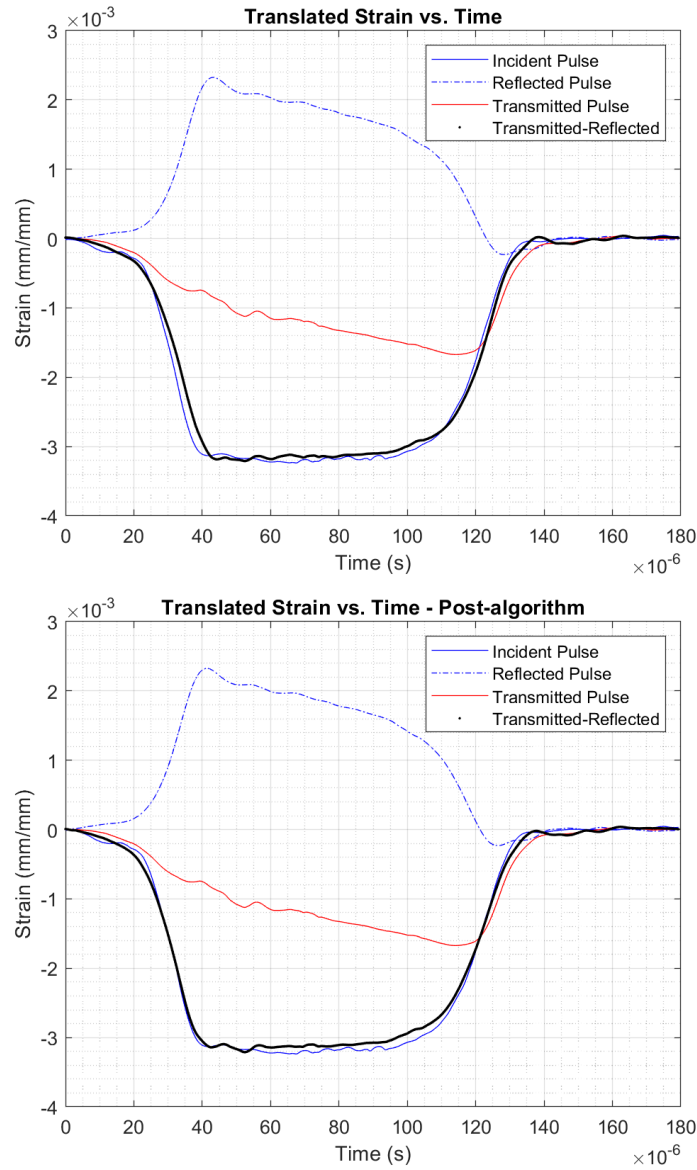
Chapter 6 – FUTURE WORK

The presented SHPB facility was designed to be used for a broad range of materials. Improvements to the design can be made to increase the breadth of capabilities as well as improve the accuracy and ease of use. The presented facility was designed to be mounted on an optical table which would improve the alignment of the pressure bars and increase the stiffness of the system. The precision surface of the optical table would also make aligning the pressure bars significantly easier potentially saving time in the future. Other modifications may be made as well such as the addition of a thermal chamber to conduct dynamic high temperature tests. A high-speed camera with a frame rate of 100,000 fps or greater could be used to image the specimen during compression. A trigger for the camera could be easily implemented with the current equipment.

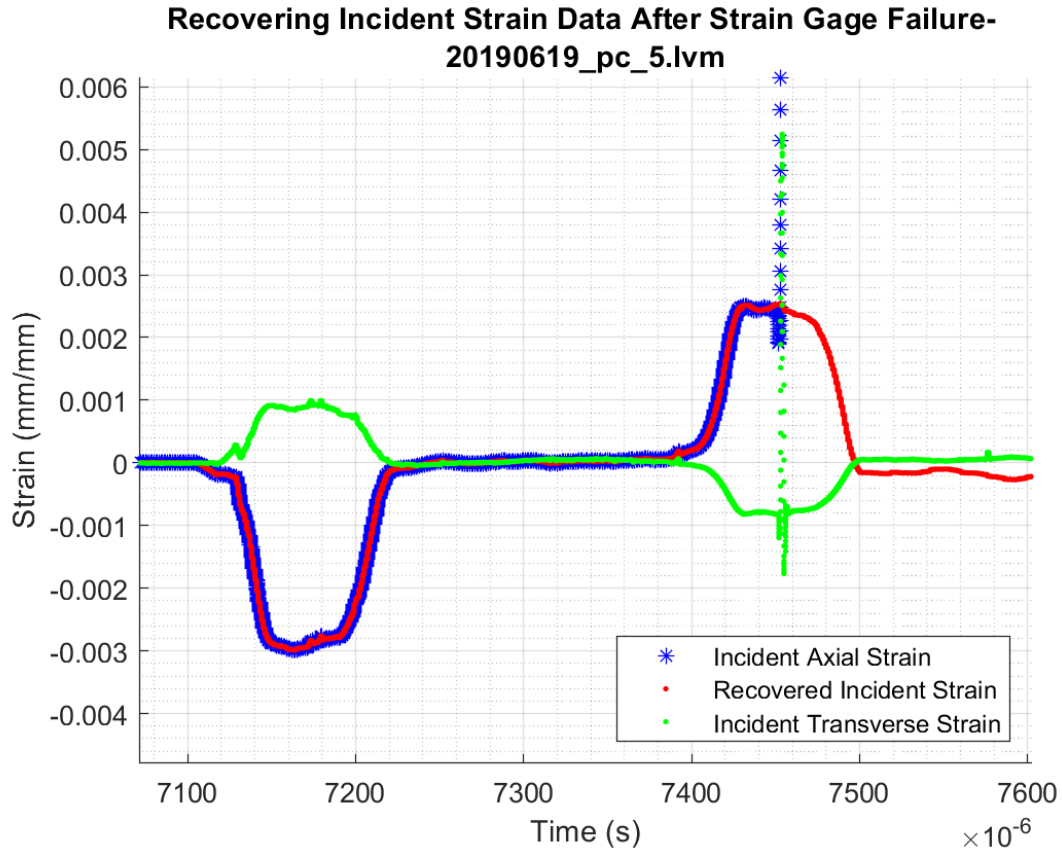
Further investigation in the use of pulse shapers, specimen design, and striker bar geometries must also be studied. Numerical correction for wave dispersion could be implemented to improve the accuracy of the results.

Only few materials have been tested using the presented SHPB facility. Investigation of the dynamic response of composite materials such as CFRP or Kevlar Reinforced Polymers may be investigated as well. Due to rapid improvement of additive manufacturing technology, many researchers are beginning to investigate the dynamic response of printed metals and polymers. Additive manufacturing will be used heavily in aerospace and defense industries, both of which will require a complete understanding of the material's mechanical response especially in the dynamic range.

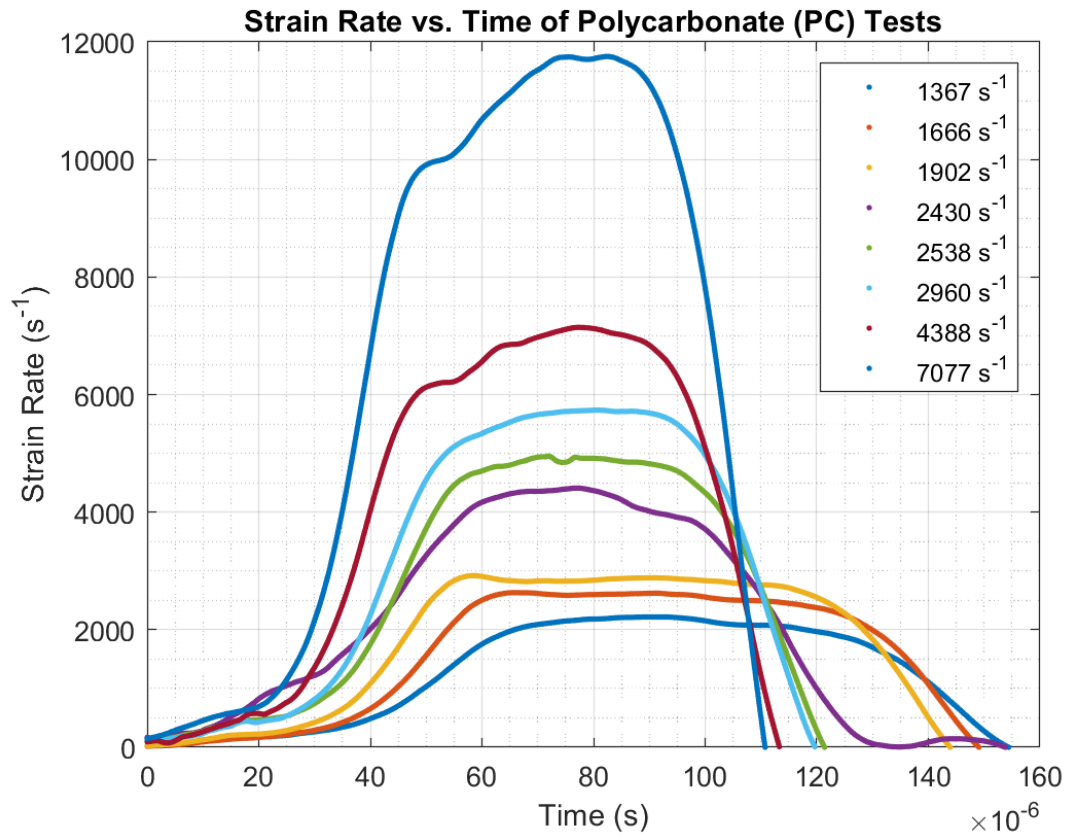
APPENDICES



A.1: Wave optimization algorithm shifts the reflected and transmitted waves to best fit the equation $\varepsilon_I = \varepsilon_T - \varepsilon_R$. The algorithm uses a least squares method. In this example, the reflected wave was shifted by $1.85 \mu\text{s}$ and the transmitted wave was shifted by $0.15 \mu\text{s}$. This improved the coefficient of determination, R^2 , from $3.0\text{e-}5$ to $8.4\text{e-}6$.



A.2: If an axial strain gage breaks during the test, the transverse strain gages may be used to approximate the axial strain. This approximation can be appended to the axial strain measurement to reproduce the data from the experiment. In this example, the axial strain gage at the peak of the reflected wave. The incident strain was reproduced using the incident transverse strain gage.



A.3: The strain rate for SHPB tests are non-constant. The strain rate ramps up in the first 40 μs , plateaus, then ramps down. The strain rate reported for the experiment is the average of the strain rate history. A test reported as 7,077 s^{-1} has a peak strain rate of 12,000 s^{-1} .

REFERENCES

1. Ramesh, K.T., *High Strain Rate and Impact Experiments*, in *Springer Handbook of Experimental Solid Mechanics*, J. Sharpe, W. N., Editor. 2008, Springer.
2. Siviour, C.R., et al., *The high strain rate compressive behaviour of polycarbonate and polyvinylidene difluoride*. *Polymer*, 2005. **46**(26): p. 12546-12555.
3. Hopkinson, B., *A Method of Measuring the Pressure Produced in the Detonation of High Explosives or by the Impact of Bullets*. *Philosophical Transactions of the Royal Society A: Mathematical, Physical and Engineering Sciences*, 1914. **213**(497-508): p. 437-456.
4. Bertholf, L.D. and C.H. Karnes, *Two-dimensional analysis of the split hopkinson pressure bar system*. *Journal of the Mechanics and Physics of Solids*, 1975. **23**(1): p. 1-19.
5. Sierakowski, R.L. and S.K. Chaturvedi, *Dynamic loading and characterization of fiber-reinforced composites*. 1997: Wiley.
6. Meyer, H.W. and D.S. Kleponis, *Modeling the high strain rate behavior of titanium undergoing ballistic impact and penetration*. *International Journal of Impact Engineering*, 2001. **26**(1-10): p. 509-521.
7. Meyer, H.W. and D.S. Kleponis, *An Analysis of Parameters for the Johnson-Cook Strength Model for 2-in-Thick Rolled Homogeneous Armor*, in *Advanced Simulation Technologies Conference; Military, Government and Aerospace Simulation, Simulation Series*. 1998.
8. Gary III, G.T., et al., *Constitutive equations for annealed metals under compression at high strain rates and high temperatures*. 1994, Los Alamos National Laboratory: Los Alamos, New Mexico.
9. Chen, W. and B. Song, *Split Hopkinson (Kolsky) Bar*. *Mechanical Engineering Series*. 2011: Springer.
10. UENISHI, A., et al., *Material Characterization at High Strain Rates for Optimizing Car Body Structures for Crash Events*, in *Nippon Steel Technical Report*. 2003.
11. Chen, Y., et al., *Stress-strain behaviour of aluminium alloys at a wide range of strain rates*. *International Journal of Solids and Structures*, 2009. **46**(21): p. 3825-3835.
12. Lang, S.M., *Design of a split hopkinson bar apparatus for use with fiber reinforced composite materials*, in *Mechanical Engineering*. 2012, Utah State University: Logan, Utah.
13. Gao, J., *Split-Hopkinson Pressure Bar Testing and Constitutive Model Evaluation for 7050-T7451 Aluminum, IN718 Superalloy, & 300M Steel*, in *Department of Mining and Materials Engineering*. 2017, McGill University.
14. REL, I. *REL's SURE-Test Systems – Hopkinson / Kolsky Bar Value Proposition*. 2019; Available from: <https://www.relinc.com/split-hopkinson-bar-kolsky-bars/shpb-value-proposition/>.
15. Kamat, A., *Design and testing of materials using split hopkinson bar*, in *Mechanical and Aerospace Engineering*. 2016, Rutgers University: New Brunswick, NJ.

16. Davies, R.M., *A Critical Study of the Hopkinson Pressure Bar*. Philosophical Transactions of the Royal Society A: Mathematical, Physical and Engineering Sciences, 1948. **240**(821): p. 375-457.
17. Kolsky, H., *An Investigation of the Mechanical Properties of Materials at very High Rates of Loading*. Proceedings of the Physical Society. Section B, 1949. **62**(11): p. 676-700.
18. Brown, L.B., et al., *Computational and Split-Hopkinson Pressure-Bar studies on the effect of the jacket during penetration of an AK47 bullet into ceramic armour*. Materials & Design, 2017. **119**: p. 47-53.
19. Nurel, B., et al., *Split Hopkinson pressure bar tests for investigating dynamic properties of additively manufactured AlSi10Mg alloy by selective laser melting*. Additive Manufacturing, 2018. **22**: p. 823-833.
20. Asgari, H., et al., *On dynamic mechanical behavior of additively manufactured AlSi10Mg_200C*. Materials Letters, 2018. **211**: p. 187-190.
21. Naghdabadi, R., M.J. Ashrafi, and J. Arghavani, *Experimental and numerical investigation of pulse-shaped split Hopkinson pressure bar test*. Materials Science and Engineering: A, 2012. **539**: p. 285-293.
22. Bagher Shemirani, A., R. Naghdabadi, and M.J. Ashrafi, *Experimental and numerical study on choosing proper pulse shapers for testing concrete specimens by split Hopkinson pressure bar apparatus*. Construction and Building Materials, 2016. **125**: p. 326-336.
23. Zhong, W.Z., et al., *Influence of interfacial friction and specimen configuration in Split Hopkinson Pressure Bar system*. Tribology International, 2015. **90**: p. 1-14.
24. Song, B., et al., *Improved Kolsky-bar design for mechanical characterization of materials at high strain rates*. Measurement Science and Technology, 2009. **20**(11).
25. Miao, Y.-G., et al., *Determination of dynamic elastic modulus of polymeric materials using vertical split Hopkinson pressure bar*. International Journal of Mechanical Sciences, 2016. **108-109**: p. 188-196.
26. Bustamante, M., D.S. Cronin, and D. Singh. *Experimental Testing and Computational Analysis of Viscoelastic Wave Propagation in Polymeric Split Hopkinson Pressure Bar*. 2018. Springer.
27. Nie, H., et al., *A versatile split Hopkinson pressure bar using electromagnetic loading*. International Journal of Impact Engineering, 2018. **116**: p. 94-104.
28. Kolsky, H., *Stress waves in solids*. Journal of Sound and Vibration, 1964. **1**(1): p. 88-110.
29. Zukas, J.A., et al., *Impact Dynamics*. 1982: Wiley.
30. Figliola, R.S. and D.E. Beasley, *Theory and Design for Mechanical Measurements*. 5 ed. 2011: Wiley.
31. *Practical Strain Gage Measurements*. 1999, Agilent Technologies.
32. Rahner, C., et al., *Numerical Evaluation of a Light-Gas Gun Facility for Impact Test*. Modelling and Simulation in Engineering, 2014. **2014**: p. 1-6.
33. Siegel, A., *The Theory of High Speed Guns*. NATO, 1965.
34. Porat, Y. and M. Gvishi, *The performance of a short-barrelled gas gun*. Journal of Physics E: Scientific Instruments, 1980. **13**(5): p. 504-505.

35. Brown, J.R., et al., *A gas-gun facility for material impact studies using low-velocity, low-mass projectiles*. Journal of Physics E: Scientific Instruments, 1989. **22**(9): p. 771-774.
36. Ravichandran, G. and G. Subhash, *Critical-Appraisal of Limiting Strain Rates for Compression Testing of Ceramics in a Split Hopkinson Pressure Bar*. Journal of the American Ceramic Society, 1994. **77**(1): p. 263-267.
37. Lok, T.S., et al., *Testing and Response of Large Diameter Brittle Materials Subjected to High Strain Rate*. Journal of Materials in Civil Engineering, 2002. **14**(3): p. 262-269.
38. Chen, W., et al., *Dynamic Compression Testing of Soft Materials*. Journal of Applied Mechanics, 2002. **69**(3).
39. Ueda, K. and A. Umeda, *Dynamic response of strain gages up to 300 kHz*. Experimental Mechanics, 1998. **38**(2): p. 93-98.
40. Oi, K., *Transient response of bonded strain gages*. Experimental Mechanics, 1966. **6**(9): p. 463-469.
41. Bagaria, W.J. and W.N. Sharpe, *Temperature and rise-time effects on dynamic strain measurement*. Experimental Mechanics, 1980. **20**(6): p. 205-210.
42. Bolduc, M. and R. Arsenault, *Development of a strain-gage installation method for high-speed impact of strikers on a Split Hopkinson bar apparatus*. EPJ Web of Conferences, 2012. **26**.
43. Smith, S.W., *The Scientist and Engineer's Guide to Digital Signal Processing*. 2 ed. 1999: California Technical Publishing.
44. Davies, E.D.H. and S.C. Hunter, *The dynamic compression testing of solids by the method of the split Hopkinson pressure bar*. Journal of the Mechanics and Physics of Solids, 1963. **11**(3): p. 155-179.
45. Lee, W.-S., et al., *The strain rate and temperature dependence of the dynamic impact properties of 7075 aluminum alloy*. Journal of Materials Processing Technology, 2000. **100**(1-3): p. 116-122.
46. Yadav, S., D.R. Chichili, and K.T. Ramesh, *The mechanical response of a 6061-T6 Al/Al₂O₃ metal matrix composite at high rates of deformation*. Acta Metallurgica et Materialia, 1995. **43**(12): p. 4453-4464.
47. Lee, W.-S., J.-C. Shyu, and S.-T. Chiou, *Effect of strain rate on impact response and dislocation substructure of 6061-T6 aluminum alloy*. Scripta Materialia, 1999. **42**(1): p. 51-56.
48. Salvado, F.C., et al., *A review on the strain rate dependency of the dynamic viscoplastic response of FCC metals*. Progress in Materials Science, 2017. **88**: p. 186-231.
49. Chichili, D.R. and K.T. Ramesh, *Dynamic failure mechanisms in a 6061-T6 Al/Al₂O₃ metal—matrix composite*. International Journal of Solids and Structures, 1995. **32**(17-18): p. 2609-2626.